Impacts of Salinity Stratification on sub-seasonal SST warming in the Northern Indian Ocean

S. Kerhalkar[1,2], A. Tandon[1], J.A. MacKinnon[3]

[1]School for Marine Science and Technology, University of Massachusetts Dartmouth, New Bedford, MA, USA

[2]School of Ocean and Earth Science and Technology, University of Hawai'i at Manoa, Honolulu, HI, USA

[3]Scripps Institution of Oceanography, University of California, San Diego, La Jolla, CA, USA

Key Points:

- Spatial variability of O(1°C) is observed during the spring intermonsoon warming in the Northern Indian Ocean.
- Salinity stratification can enhance or suppress surface warming by up to 0.5°C, depending on heat fluxes and water optics.
- The daily-averaged heat flux value where salinity stratification begins to amplify surface warming is quantified (Q_{cross}).

Corresponding author: Siddhant Kerhalkar, siddhant@hawaii.edu

Abstract

The Northern Indian Ocean (NIO) experiences strong upper ocean warming during the spring intermonsoon season, with nearly 90% of the days showing net heat gain. However, observations reveal spatially heterogeneous Sea Surface Temperature (SST) trends [O(1 °C) differences] in these regions over intra-seasonal timescales (15-45 days) and mesoscale and smaller length scales (< 100 km), coinciding with significant lateral variability in winds [O(2 $\mathrm{m\,s^{-1}}$)] and salinity stratification [O(2 $\mathrm{g\,kg^{-1}}$) in surface salinity and O(20 m in mixed layer depth)]. This study investigates the role of salinity-driven mixed layers in driving these gradients in foundational SST warming using one-dimensional modeling. Simulation results using realistic surface forcing show that lateral differences in stratification result in spatial differences in warming of foundational SST by about 0.2-0.5°C over 14-21 days, specifically for shallow mixed layers. However, the influence of stratification on foundational SST warming is nuanced and varies across the NIO, leading to either enhanced or reduced warming. Idealized simulations show that this contrast depends on net heat flux and water optical properties, with stratified cases warming more under high fluxes and turbid conditions. To generalize, we derive an analytical expression for the crossover heat flux (Q_{cross}), the threshold daily-averaged net heat flux value at which stratified and unstratified cases warm equally. Q_{cross} depends on shortwave radiation, mixed layer depth, and optical properties. For representative clear-sky conditions, Q_{cross} ranges from 103 to 136 $\mathrm{W\,m^{-2}}$. These findings underscore the role of salinity-driven stratification and bio-optical feedback in shaping SST gradients, with likely implications for sub-seasonal to seasonal monsoon forecasting.

Plain Language Summary

The Northern Indian Ocean undergoes intense surface warming during the spring intermonsoon season, prior to Monsoons. Observations reveal that the warming trend in the surface temperatures is spatially uneven over intra-seasonal timescales (15-45 days) and shorter length scales (< 100 km). This variability coincides with significant lateral differences in wind speeds and salinity stratification. Our study shows that in shallow mixed layers, riverine-driven salinity stratification strongly influences surface warming differences. Interestingly, the impact of salinity stratification on surface warming are found to be varying in the NIO, leading to either enhanced or reduced warming. Idealized simulation results provide evidence that this difference is due to the sensitivity of surface

warming nature to net heat flux and water optics. Under higher heat flux and more murkier conditions, stratified cases warm more. We also derive a theoretical daily-averaged net heat flux value at which stratified and unstratified scenarios result in the same SST warming rate. This threshold ranges from 103 to 136 $\mathrm{W\,m^{-2}}$ under typical clear-sky conditions and tropical open-ocean waters, depending on water clarity and mixed layer depth. These results highlight the importance of salinity-driven stratification and bio-optical feedback in modulating regional SST evolution, factors that can influence tropical cyclone intensity and monsoon predictability.

1 Introduction

A precursor to the onset of Monsoons and their associated high wind speeds and rainfall is the presence of warm waters in the Northern Indian Ocean (NIO) during the spring intermonsoon season (Vinayachandran & Shetye, 1991; Rao & Sivakumar, 1999). Conditions in the NIO during this period are characterized by clear skies with net surface heat fluxes of O(100 $\mathrm{W\,m^{-2}}$) and wind speeds below 6 $\mathrm{m\,s^{-1}}$ (Weller et al., 1998, 2019). Such conditions increase the foundational sea surface temperature (SST), denoted as T_f hereafter and defined as the component of SST that varies on timescales longer than the diurnal cycle (see Section 2.4 of this paper for more details on T_f), by approximately 3–4°C (Weller et al., 1998, 2019). The conditions during the spring intermonsoon season also lead to high diurnal SST amplitudes and possible Diurnal Warm Layer (DWL) formation (Stuart-Menteth et al., 2003; Clayson & Weitlich, 2007; Shenoi et al., 2009; Thompson et al., 2019). The heat budget during this period is largely one-dimensional, driven by surface heat fluxes and characterized by negligible lateral heat advection and low eddy kinetic energy (Weller et al., 2002; Thangaprakash et al., 2016; Sun et al., 2022). Studies have shown that these persistent warm waters (the NIO Mini-Warm Pool) as well as the DWL presence serve as a source for atmospheric convection over diurnal and intraseasonal timescales (Rao et al., 2015; de Szoeke et al., 2021). These air-sea interactions influence pre-Monsoon tropical cyclones as well as the onset and evolution of the Monsoon (Rao & Sivakumar, 1999; Balaguru et al., 2012; Sijikumar & Rajeev, 2012; Pradhan et al., 2022).

Prior to the one-dimensional heating of the NIO during the spring intermonsoon period, it is also uniquely influenced by the seasonal discharge of river water from the Bay of Bengal (East Basin in the NIO), with peak discharge in August and September

(Sengupta et al., 2006; Jarugula et al., 2024). Mesoscale eddies, Ekman currents and the East India Coastal Current redistribute this riverwater throughout the Bay of Bengal, extending its influence to the Southern Bay (Rao & Sivakumar, 2003; Sengupta et al., 2006, 2016; Sree Lekha et al., 2018; Chaudhuri et al., 2021; Jarugula et al., 2024). This freshwater modifies the vertical stratification by forming salinity-stratified mixed layers (or barrier layers) and creating salinity fronts over O(10 km) (Sengupta & Ravichandran, 2001; Shenoi et al., 2002; Rao & Sivakumar, 2003; Sengupta et al., 2006; Mahadevan et al., 2016; Sengupta et al., 2016; Wijesekera et al., 2016; Sree Lekha et al., 2018; Hormann et al., 2019; Sree Lekha et al., 2020). The East India coastal current, along with coastally trapped Kelvin waves and downwelling Rossby waves, facilitate the freshwater exchange between the Bay of Bengal and the Arabian Sea (west basin in the NIO, Rao & Sivakumar, 2003; Vinayachandran & Nanjundiah, 2009; Rao et al., 2010; Hormann et al., 2019). This exchange alters the vertical stratification in the Arabian Sea prior to the spring intermonsoon season as well (Sprintall & Tomczak, 1992; Echols & Riser, 2020).

The presence of such shallow salinity-stratified mixed layers enhances diurnal SST amplitudes in the NIO region (Moshonkin & Harenduprakash, 1991; Shroyer et al., 2016; Kerhalkar et al., 2025b). These layers significantly modulate the upper ocean heat budget by inhibiting vertical mixing of cooler subsurface waters, allowing heat to accumulate near the surface and promoting T_f warming (Moshonkin & Harenduprakash, 1991; Yuan et al., 2020). At the same time, these layers can also lead to an increased escape of penetrative heat fluxes to deeper waters (due to penetrative shortwave radiation) by a factor of 3 (Sengupta et al., 2008). This effectively reduces the heat retained within the mixed layer, thereby limiting the T_f warming or even cause T_f cooling (Vinayachandran et al., 2007; Sengupta et al., 2008; Echols & Riser, 2020). Due to these competing effects, there remains a lack of consensus on the role of salinity-stratified mixed layers in T_f evolution during the spring intermonsoon, with limited observational studies suggesting their influence on T_f evolution may be minimal (Echols & Riser, 2020).

Building on the ambiguity regarding the role of salinity stratification in modulating T_f evolution one-dimensionally, lateral variability in salinity stratification also has the potential to further generate SST fronts (e.g., Moshonkin & Harenduprakash, 1991). An existing salinity front generated prior to spring-intermonsoon period could either experience density enhancement or develop density compensation across the front, depending on how salinity stratification impacts the evolution of T_f. Quantifying such spatial

inhomogeneities in T_f evolution over mesoscale and smaller lengths is essential as it can influence local and large-scale air-sea interactions (e.g., Skyllingstad et al., 2007; Seo et al., 2023). These aspects remains largely unexplored due to lack of concurrent, high-vertical resolution in-situ observations at mesoscale and smaller length scales (< 100 km) in this data-sparse region (Beal et al., 2020; Phillips et al., 2021).

To address this gap, we use a combination of remote sensing, 1-D ocean modeling and surface forcing derived from two in-situ moorings in the NIO (one each in the Northern Bay and South-Eastern Arabian Sea) to answer the following questions:

- What are the typical differences in the warming trends of T_f across mesoscale and smaller lengths during the existence of the mini-warm pool?
- How does salinity stratification differences contribute in causing lateral differences in T_f evolution?
- Does the presence of salinity stratification suppress or accelerate the T_f warming? How does this depend on surface forcing conditions like optical properties of water, wind speeds, and heat fluxes?

We first describe the remote sensing, observational datasets and 1-D model used in this study (Section-2). Next, we describe the extent of lateral variability in SST trends and surface salinity from remote sensing (as a proxy for differences in salinity stratification) in the NIO (Section-3). The role of salinity stratification in causing the differences in T_f warming in the Northern Bay of Bengal (NBoB) and South-Eastern Arabian Sea (SEAS) is considered next, using 1-D model forced with realistic surface forcing from in-situ moorings (Section-4). We then use 1-D model with idealized forcing conditions to isolate the differences in action of salinity stratification on T_f warming trends (Section-5). Finally, we develop an analytical expression to explain the role of salinity stratification in the evolution of T_f (Section-6). The broader implications of this research are discussed in Section 7, with a summary of findings in Section 8.

2 Data and Methods

2.1 In-Situ Sources

In this study, we use surface meteorological variables and COARE-derived bulk fluxes (Fairall et al., 1996a, 2003; Edson et al., 2013), together with SST and subsurface tem-

perature and salinity measurements from the AD08 and ASIRI moorings. The AD08 mooring in the SEAS (located at 11.7°N and 68°E, Blue star in Figure 1a) is one of the long-term operational sites maintained by the India's National Institute of Ocean Technology (NIOT, Joseph et al., 2022). We derive bulk fluxes using COARE 3.6 with hourly observations at the AD08 mooring. Temperature and salinity at AD08 mooring were measured at depths of 1, 5, 10, 15, 20, 30, 50, 75, 100, 200, and 500 m. Our analysis uses the data from February to May 2018, corresponding to the spring intermonsoon season (Weller et al., 1998).

The ASIRI mooring was deployed by the Woods Hole Oceanographic Institution (WHOI) for the ASIRI (Air–Sea Interactions in the Northern Indian Ocean, Wijesekera et al., 2016) field campaign in the NBoB (located at 18.0°N, 89.5°E, Green star in Figure 1a) between December 2014 and January 2016. COARE 3.0 algorithm is used to derive bulk fluxes from the 1-minute time resolution observations at this site (The use of different bulk flux algorithms at the AD08 and ASIRI moorings reflects only the timing of the respective analyses, not a scientific rationale, and they should yield similar results; pers. comm., Elizabeth Thompson). The ASIRI mooring is also instrumented with 15 Sea-Bird SBE 37 CT sensors distributed through the upper 100 m, recording internally every 15 minutes. We use data from February to May 2015, also representing the spring intermonsoon season (Weller et al., 2016). Further details on the instrumentation and measurements at the AD08 and ASIRI moorings can be found in Joseph et al. (2022), Weller et al. (2016) and Weller et al. (2019).

To assess the typical mixed layer depths (MLDs) around the AD08 and ASIRI moorings in the SEAS and NBoB, respectively, we use ARGO float profiles (Roemmich et al., 2009). Profiles are selected within a $3^\circ \times 2^\circ$ box centered around AD08 and the ASIRI moorings. The analysis is restricted to the spring intermonsoon season for years 2003 to 2024.

2.2 Remote Sensing

To examine the spatial variations in T_f and its changes, we utilize NOAA 0.09° Daily Optimum Interpolation Sea Surface Temperature (OISST, Reynolds et al., 2007). This is a level-3 blended product combining microwave and infrared data, at a spatial resolution of nearly 9 km. For understanding the spatial differences in the sea surface salin-

ity (SSS), we use Soil Moisture Active Passive mission (SMAP) data. Although gridded at a 25 km scale, its effective spatial resolution is 47 km (Brown et al., 2013). Daily wind data is obtained from the Advanced Microwave Scanning Radiometer 2 (AMSR-2) aboard the AQUA satellite. Daily wind measurements from AMSR-2 are available at an effective resolution of 46 km, despite being gridded to a 25 km scale as well (Wentz et al., 2014). Our analysis spans the period from 01 March to 30 April 2018 as to overlap with availability of observations at the AD08 mooring.

2.3 Models

The General Ocean Turbulence Model (GOTM) is a one-dimensional ocean model framework that includes various vertical mixing schemes (Burchard et al., 1999). GOTM also provides options for selecting stability functions, as well as parameterizations for wave breaking and internal waves. The k–ϵ turbulence closure scheme within GOTM parameterizes subgrid-scale turbulent kinetic energy (k) and its dissipation rate (ϵ), with both variables evolved using separate prognostic transport equations. This scheme has been employed in previous studies to model the upper ocean (e.g., Johnson et al., 2023a; Burchard et al., 2002; Drushka et al., 2016). In this study, we use the k–ϵ mixing scheme along with the dynamic dissipation rate length scale and the Canuto A version of the stability function (Canuto et al., 2001). We adopted GOTM's default settings, omitting only the internal wave breaking parameterization (Burchard et al., 1999).

We conduct two suites of simulations: one forced with realistic surface fluxes from mooring observations (run over the periods described in Section 4), and another using idealized surface forcing (run for 30 days, as outlined in Section 5). All simulations are initialized near sunrise (00:00 UTC) and use vertical and temporal resolutions of 0.05 m and 1 minute, respectively. Additional details on the initial and forcing conditions for these simulations are provided in Sections 4 and 5.

2.4 Quantifying T_f

We define the foundational temperature (T_f) as the near-surface temperature (0.5 m depth) immediately before sunrise each day, following the convention that this predawn state is least affected by diurnal warming or nocturnal cooling (Donlon et al., 2007; Prytherch et al., 2013). We obtain T_f once per local day (00:00 UTC to 00:00 UTC) to

isolate variability on time scales longer than the diurnal cycle (similar to the approach in Prytherch et al., 2013; Kerhalkar et al., 2025b). While our primary processes of interest are the daily cycles of heating and cooling, our focus is on their cumulative impacts. Therefore, changes in T_f from one sunrise to the next are used to quantify longer-term modulation of the upper-ocean thermal state.

3 Observed spatial variability in T_f, SSS, Winds and MLDs during Spring intermonsoon season

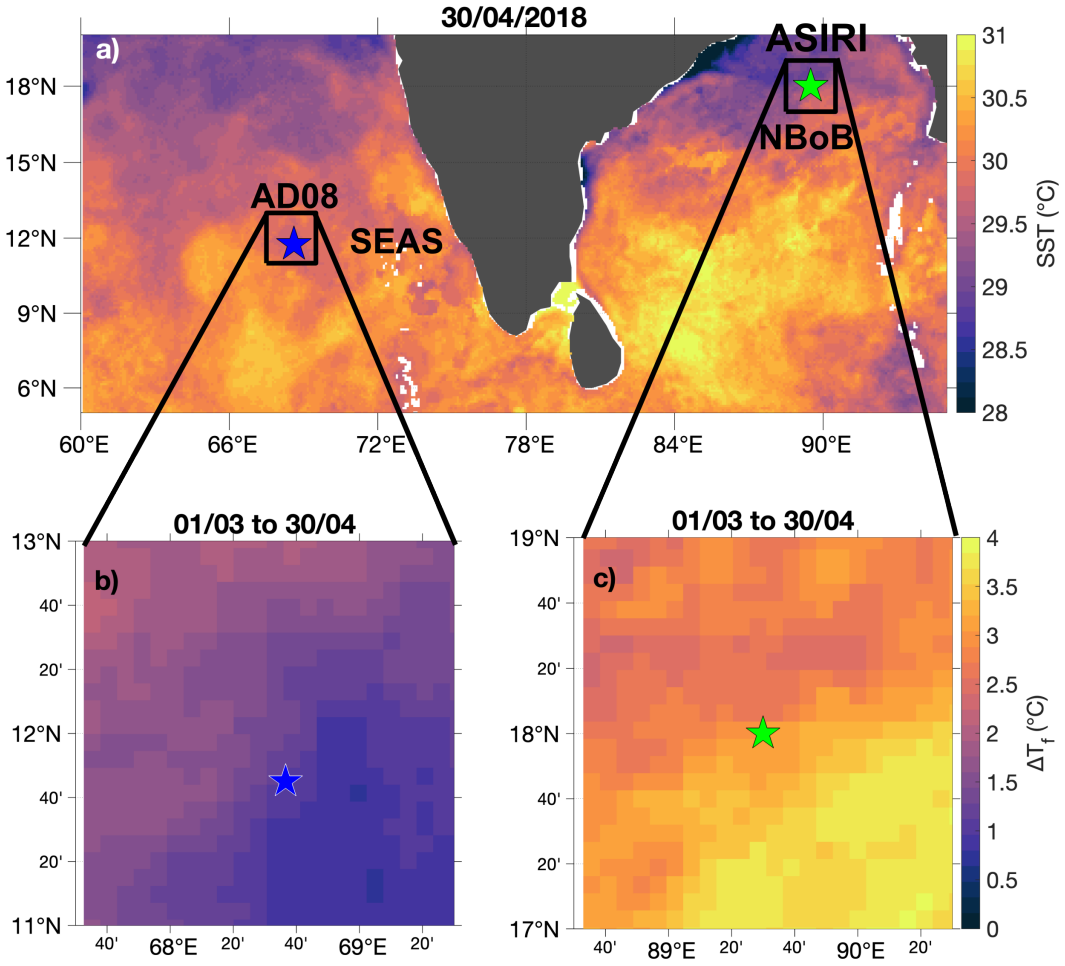

Figure 1. (a) SST of the Northern Indian Ocean on 30 April 2018 from OISST. The blue and green stars indicate the AD08 mooring in SEAS and ASIRI Mooring in NBoB respectively. (b) and (c) Change in T_f from 01 March to 30 April 2018 within the boxes in vicinity of the moorings as indicated in (a).

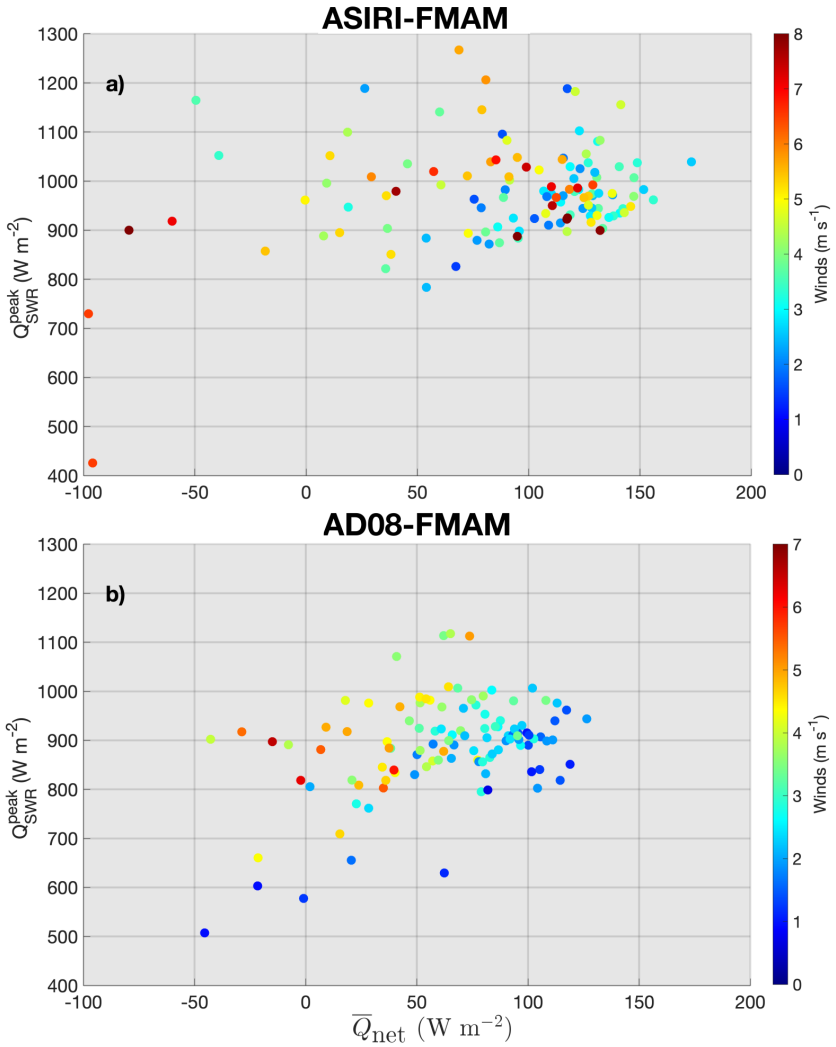

Figure 2. (a) Scatter plot of daily peak shortwave radiation (Q^{peak}_{SWR}, y-axis) vs. daily mean net heat flux ($\overline{Q_{net}}$, x-axis) from the ASIRI mooring in the NBoB during February-May 2015, with colors indicating the daily mean wind speed. (b) is the same as (a) but for AD08 mooring in the SEAS during February-May 2018.

Satellite SST measurements from the 2018 spring intermonsoon season show the NIO warming to above 29°C by the end of April (Figure 1a), creating conditions favorable for atmospheric convection (e.g., Gadgil, 2003). The corresponding increase in the foundational temperature (ΔT_f) over the months of March and April ranges from 1 to 4°C (equivalent to 0.5–2°C per month), with higher ΔT_f values in NBoB compared to the SEAS (Figure 1b,c). This regional difference within the NIO is likely driven by differences in net surface heat fluxes, which are higher by O(50 W m^{-2}) in the NBoB than

in the SEAS (Figure 2). This occurs despite largely clear skies and similar shortwave radiation (SWR) in both regions. Over 90% of the days during this period exhibit positive net heat fluxes, supporting the overall warming trend.

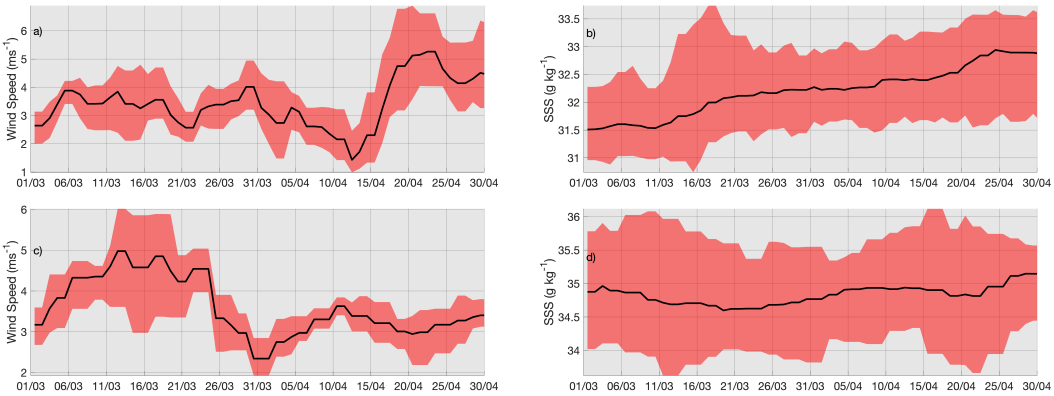

Figure 3. (a) Time series of the mean wind speed (black line) over the box in the NBoB (Figure 1c), with the range of values shown in red shade between 01 March and 30 April 2018. (b) Same as (a) but for SSS over the box in Figure 1c. (c) and (d) are the same as (a) and (b) over the box in SEAS (Figure 1b).

Beyond basin-wide differences, satellite SST also reveals O(1°C) spatial variability in $\Delta\, T_f$ over mesoscale and smaller lengths (< 100 km) within both NBoB and SEAS (Figure 1b,c). While such variability suggests partial influence of spatial variability in the net heat fluxes over mesoscale and smaller lengths, reliable estimates of this variability are not available from coarser remote sensing and reanalysis products. However, wind speeds in both regions during this period show spatial variability of O(2 $\mathrm{m\,s^{-1}}$) over mesoscale and smaller lengths (Figure 3a,c), with nearly similar spatially averaged wind speeds in both the regions (except between 15-30 April, where the NBoB has stronger winds by about 2 $\mathrm{m\,s^{-1}}$). These spatial differences in winds suggests a potential contribution to unresolved small-scale variability in surface heat fluxes.

Past studies indicate that salinity stratification significantly modifies SST and the upper ocean heat budget as well (Sengupta et al., 2008; Yuan et al., 2020). Satellite SSS measurements reveal enhanced spatial variability of O(2 g/kg) over mesoscale and smaller lengths in both NBoB and SEAS regions, with NBoB being consistently fresher than SEAS (Figure 3b,d). Because salinity gradients at submesoscale and smaller mesoscale lengths are much weaker beneath the mixed layer (e.g., Jaeger & Mahadevan, 2018), surface salin-

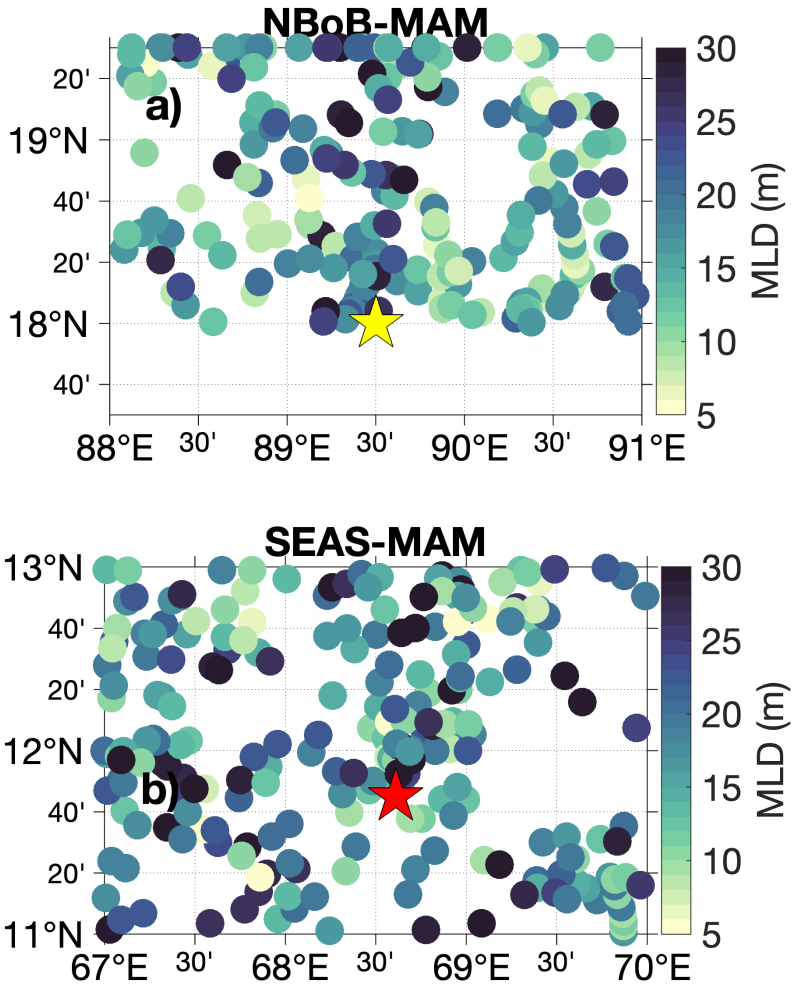

Figure 4. (a) MLDs inferred from ARGO floats in a 3° × 2° centered around the ASIRI mooring (in yellow star) in the NBoB for months of March, April and May between 2003 and 2024. (b) is the same as (a) but for a similar region around the AD08 mooring (in red star) in the SEAS.

ity gradients serve as a useful proxy for lateral differences in salinity-driven stratification. Additionally, long-term ARGO float analysis highlights that MLDs are found to be varying between 5-30 m in NBoB and SEAS during the spring intermonsoon season (Figure 4).

While spatial gradients in ΔT_f are observed to be as high as 2°C, quantifying the causes of these observed spatial ΔT_f differences solely through observations is challenging. Therefore, we employ an idealized one-dimensional (1-D) modeling approach to specif-

243 ically explore how lateral differences in salinity stratification drive lateral variations in
244 ΔT_{f}.

245 4 1-D modeling experiments using observed surface forcing in NIO

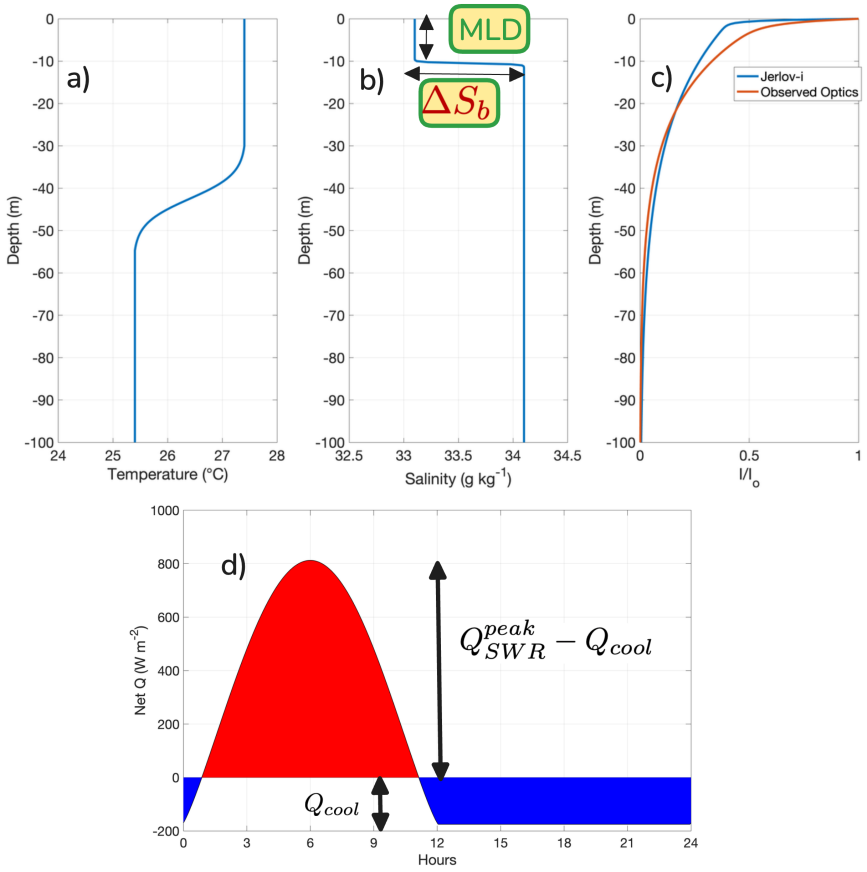

Figure 5. Initial vertical profiles of (a) temperature, (b) salinity and (c) ratio of downward irradiance (I) to incident irradiance at the surface ($\mathrm{I_o}$), for the GOTM parameter space exploration. The temperature and salinity in the upper layer is set using the initial SST and SSS respectively. Stratification in the initial profiles is controlled using the MLD and the initial change in salinity at the base of mixed layer (ΔS_b). (d) A typical diurnally varying idealized forcing flux is shown as a function of time in UTC for Indian Ocean, with a constant cooling component of flux (i.e., sum of net longwave radiation, latent heat flux, and sensible heat flux, which typically cool the Indian Ocean, Q_{cool}) and diurnally varying SWR that peaks during the day (Q_{SWR}^{peak})

246 GOTM simulations are forced with high-resolution surface fluxes and wind speeds
247 from the ASIRI and AD08 moorings to understand the role of salinity stratification in

causing lateral variations in ΔT_f. Simulations are initialized with idealized temperature and salinity profiles inspired by past observations from these regions. The upper layer's temperature and salinity are set using the initial SST and SSS observed at the respective moorings (Figure 5a,b). Upper ocean stratification is controlled by the initial MLD at sunrise and the initial salinity change at the base of the MLD (ΔS_b). Additionally, a 2°C change in temperature over 10 m is assumed at a depth of 40 m to emulate a typical thermocline. We model the penetration of solar radiation using a double exponential decay with attenuation coefficients appropriate for Jerlov-I water type (Figure 5c, Paulson & Simpson, 1977).

During a 21-day period between 08 March and 01 April 2015 in the NBoB, consistent wind speeds below 6 $\mathrm{m\,s^{-1}}$ (Figure 6a) favor DWL formation (Thompson et al., 2019; Kerhalkar et al., 2025b). Consistent with this, observations show a clear diurnal cycle in SST accompanied by the formation of DWLs in the upper ocean (Figure 6b,e). The observed ΔT_f during this 21-day period is 2.2°C(Figure 6b). A simulation assuming no salinity stratification in the initial profile yields a ΔT_f of 2.1°C, with consistent upper ocean warming (down to 25 m depth) and presence of DWLs (Figure 6b,c). The modeled upper-ocean temperature evolution closely resembles the observed evolution, aside from high-frequency variability in the observations likely due to internal wave activity (Figure 6e, e.g., Chaudhuri et al., 2019). In contrast, using salinity-stratified initial conditions (initial MLD=6 m and ΔS_b=1 $\mathrm{g\,kg^{-1}}$) increases the ΔT_f by 0.4°C (to 2.5°C, Figure 6b,d). Presence of enhanced stratification traps the DWLs and the associated heat distribution to shallower depths (Figure 6d). Comparison of resulting model temperature profiles reveal that the non-salinity-stratified scenario warms more for the first part of the period (till 17 March) at the surface (Figure 6f). In contrast, the salinity-stratified case warms more below its initial MLD when compared to the non-salinity-stratified case during this period (both cases warm in an absolute sense but differ in relative heating). This is a combined effect of surface cooling concentrated within a shallow MLD (leading to more cooling) and penetrative heat fluxes warming the sub-surface without the typical cooling at the end of the day (which happens in the non-salinity-stratified case; e.g., Sengupta et al., 2002). Conversely, the surface in salinity-stratified scenario warms more for the second part of the period (from 20 March) by trapping heat to a shallower depth (Figure 6f). As a result, the sub-surface is warmer for non-salinity-stratified case when compared to the salinity-stratified case during this period. Similar results from other

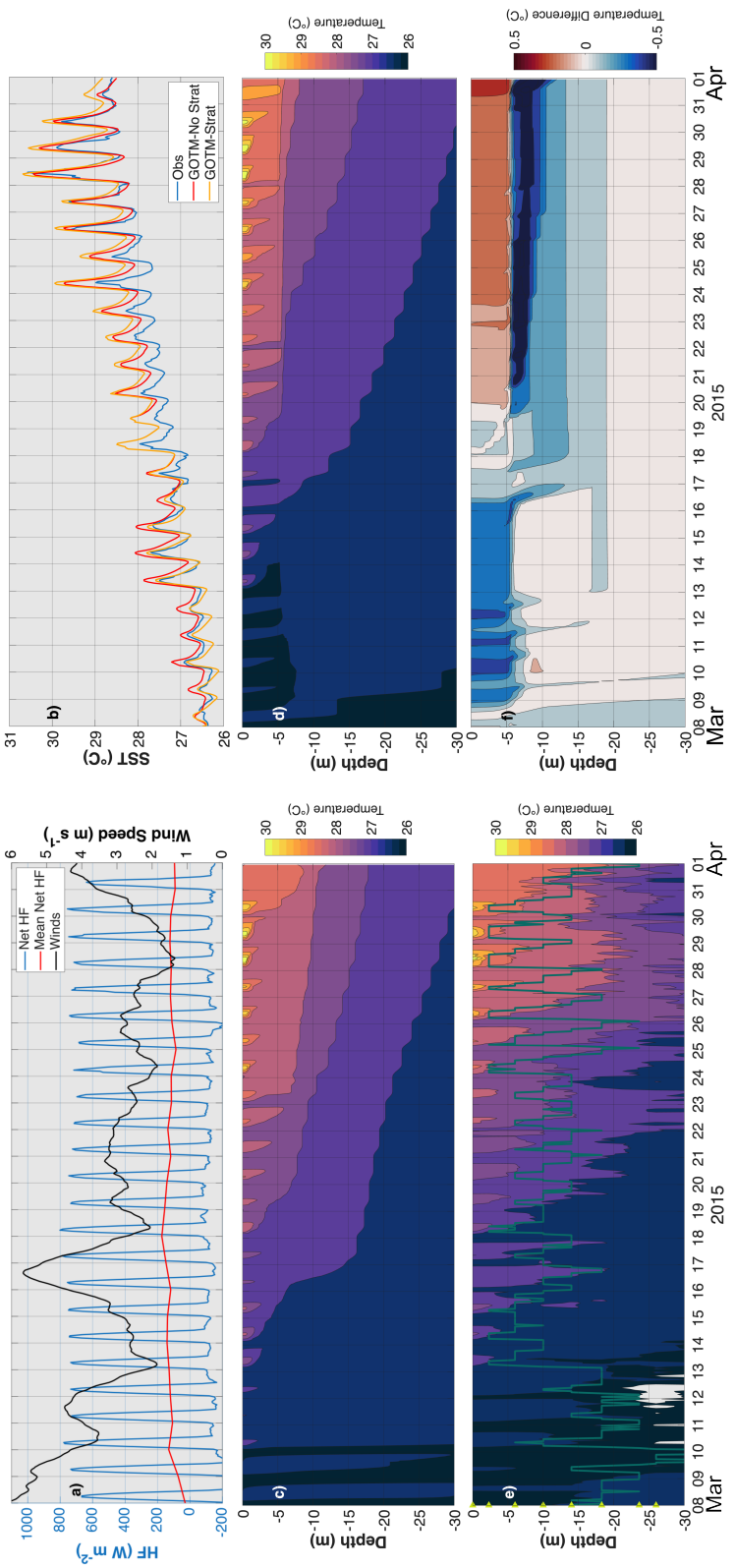

Figure 6. (a) Observed Net Heat Flux (Net HF, in blue) and its Daily Mean Net Heat Flux (Mean Net HF, in red) from ASIRI mooring in NBoB between 08 March and 01 April 2015. 24-hour smoothed wind speed at the ASIRI mooring is shown in black line with its axes limits on the right. (b) Observed SST from ASIRI mooring in NBoB (in blue), modeled SST assuming no salinity stratification (in red) as well as modeled SST assuming an initial MLD=6 m and ΔS_b=1 g kg^{-1} (in yellow) for the same time period. (c) Modeled temperature profiles assuming no salinity stratification (ΔS_b=0) for the same time period. (d) is the same as (c) but assuming an initial MLD= 6 m and ΔS_b=1 g kg^{-1}. (e) Observed Temperature profiles from ASIRI mooring for the same time period, with dark green lines indicating the MLD using a 0.125 kg m^{-3} density criteria (The MLD estimate is noisy due to the discrete depth spacing of the sensors). The light green markers at the left end of the panel indicate the depths where the measurements were taken. (f) Difference in temperature between (d) and (c). Red color indicates that the salinity-stratified case in (d) is warmer than non-salinity-stratified case in (c).

periods in April and May 2015 in NBoB reveal that the surface in case of salinity-stratified scenarios demonstrates periods of both enhanced and reduced warming when compared to non-salinity-stratified scenarios (Figure S1,S2, see upcoming section for more detailed discussions).

Observations from the AD08 mooring in the SEAS during a 15-day period (from 26 April to 10 May 2018) also show consistently low wind speeds, similar to the NBoB case discussed earlier (Figure 7a). Here, the observed ΔT_f is 0.64°C (Figure 7b). The non-salinity stratified scenario (similar to above) reveals a 0.65 °C ΔT_f, but the salinity-stratified scenario results in a lower ΔT_f of 0.45°C (Figure 7b). Although DWLs are also present in these cases (Figure 7c,d) and resembles the observed temperature profiles at AD08 mooring (Figure 7e), the surface of non-salinity stratified scenario is consistently warmer in the case of SEAS (Figure 7f). Thus SEAS and NBoB show contrasting results.

To comprehensively understand the role of salinity stratification on ΔT_f, we conduct multiple GOTM simulations with varying initial MLD (2-15 m) and ΔS_b (0-1 $\mathrm{g\,kg^{-1}}$), using the same surface forcing as discussed previously. These experiments reaffirm our earlier findings: in the SEAS scenario, enhanced stratification leads to a reduction in ΔT_f (Figure 8a). This effect is more pronounced for higher ΔS_b (> 0.8 $\mathrm{g\,kg^{-1}}$) and shallower initial MLDs (< 8 m), with differences of about 0.2°C in ΔT_f as a result. Conversely in the NBoB scenario, enhanced stratification results in a higher ΔT_f (Figure 8b). Similar to the SEAS scenario, this effect in the NBoB is more pronounced over shallow initial MLDs (< 6 m) and enhanced ΔS_b (> 0.7 $\mathrm{g\,kg^{-1}}$), resulting in differences of about 0.5°C in ΔT_f. Crucially, our detailed exploration of the NBoB scenario across its two distinct periods (discussed above) reveals contrasting results, with stratified scenarios leading to lower and higher ΔT_f values for the respective periods (Figure S3).

Overall, our 1-D simulations using observed surface forcing from the NBoB and SEAS demonstrate that salinity stratification can contribute up to 0.5°C of spatial variability in ΔT_f. This exercise suggests that the observed spatial gradients in ΔT_f are partly driven by salinity stratification, with additional influence from variability in optical properties and surface heat fluxes. These results imply that salinity stratification has contrasting impacts on ΔT_f: in presence of surface warming, a salinity front could experi-

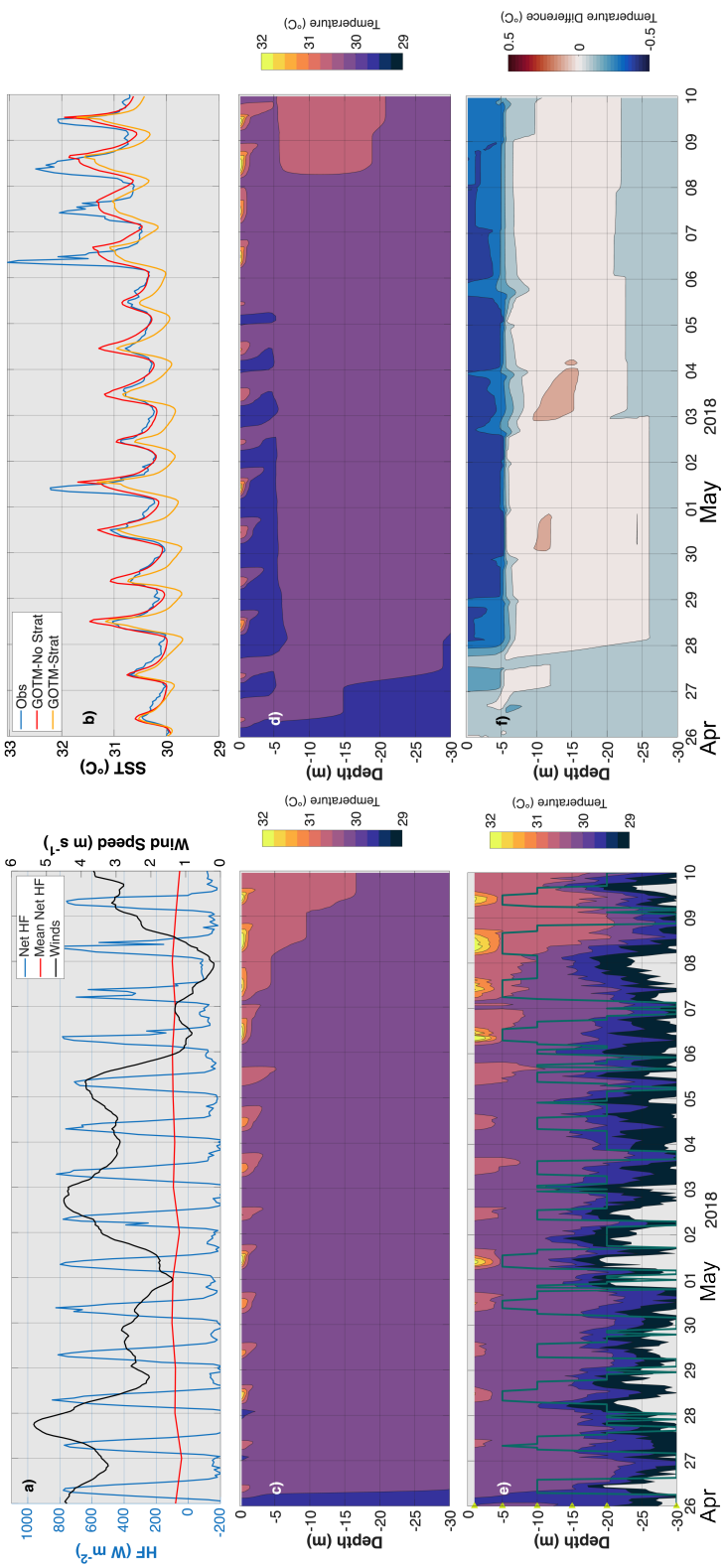

Figure 7. (a) Observed Net Heat Flux (Net HF, in blue) and its Daily Mean Net Heat Flux (Mean Net HF, in red) from AD08 mooring in SEAS between 26 April and 10 May 2018. 24-hour smoothed Wind speed at the AD08 mooring is shown in black line with its axes limits on the right. (b) Observed SST from AD08 mooring in SEAS (in blue), modeled SST assuming no salinity stratification (in red) as well as modeled SST assuming an initial MLD of 6 m and ΔS_b of 1 g kg^{-1} (in yellow) for the same time period. (c) Modeled temperature profiles assuming no salinity stratification for the same period. (d) is the same as (c) but assuming an initial MLD of 6 m and ΔS_b of 1 g kg^{-1}. (e) Observed Temperature profiles from AD08 mooring for the same time period, with dark green lines indicating the MLD using a 0.125 kg m^{-3} density criteria (The MLD estimate is noisy due to the discrete depth spacing of the sensors). The light green markers at the left end of the panel indicate the depths where the measurements were taken. (f) Difference in temperature between (d) and (c). Red color indicates that the salinity-stratified case in (d) is warmer than non-salinity-stratified case in (c).

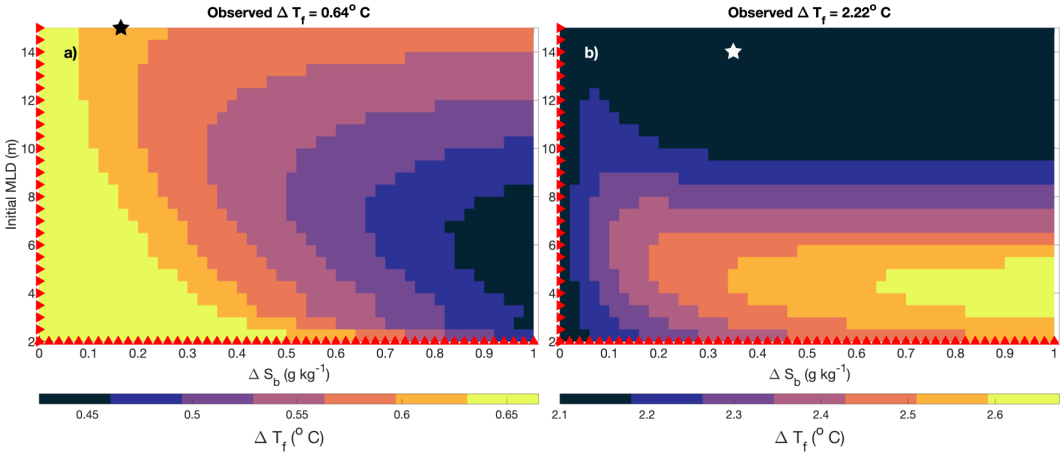

Figure 8. (a) Modeled ΔT_f between 26 April and 10 May 2018 as a function of ΔS_b (x-axis) and initial MLD (y-axis), forced with observed air-sea fluxes and wind speeds at AD08 mooring in SEAS. The observed value of ΔT_f during the same period is indicated in the sub-title, while the star marker indicates the observed value of ΔS_b and initial MLD (NOTE: Values of observed MLD and ΔS_b in the star marker are derived from discrete, coarse-resolution mooring sensors). (b) is the same as (a) but for ASIRI mooring in NBoB between 08 March and 01 April 2015. The red markers at axes indicate the different parameters for which the simulations are performed.

ence either enhanced or compensated density gradients. We resolve this conundrum in the next section.

5 1-D modeling experiments using idealized surface forcing

We adapt the heat budget framework from Rudnick and Weller (1993) to estimate ΔT_f, neglecting lateral advection and entrainment terms:

$$\Delta T_f = \frac{\int (F(H).Q_{SWR} - Q_{cool})dt}{\rho c_p H} \quad (1)$$

Here, $F(H)$ represents the fraction of SWR trapped within an effective MLD of H (dependent on the optical properties of water). Q_{SWR} and Q_{cool} represent the shortwave and cooling components of heat flux (i.e., sum of net longwave radiation, latent heat flux, and sensible heat flux, which typically cool the Indian Ocean) respectively. ρ, c_p indicate the density and specific heat capacity of water (assumed as 3991 $\mathrm{J\,kg^{-1}\,K^{-1}}$). Physically, equation 1 represents the time-integrated vertical divergence of the surface heat flux over the effective mixed layer (H), normalized by ρc_p, such that changes in T_f arise from the cumulative imbalance between absorbed shortwave heating and surface cool-

ing over time (We define negative divergence, or convergence, in the mixed layer as net heat flux into the mixed layer). While the focus is on the evolution of T_f, we note that its variability is fundamentally driven by the diurnal cycle of heat fluxes (and hence the integration over time in equation 1).

A key element of the heat budget formulation in equation 1 is the definition of the effective MLD (H), which represents the effective vertical extent over which surface heat fluxes are mixed and contribute to ΔT_f. For unstratified ($\Delta S_b = 0$) cases, vertical mixing is governed primarily by wind-driven turbulence. Under these conditions, surface heating and cooling are distributed over a wind-driven trapping depth that characterizes the vertical extent of turbulent mixing over a diurnal cycle. For a representative wind speed of 5 $\mathrm{m\,s^{-1}}$, this trapping depth is estimated to be 13.4 m (based on the formulation of Fairall et al., 1996b). In the absence of salinity stratification, this wind-driven trapping depth therefore defines the effective MLD (H) in equation 1. In contrast, when salinity stratification is present ($\Delta S_b > 0$), buoyancy effects suppress vertical mixing and limit the penetration of wind-driven turbulence as long as the initially prescribed MLD due to salinity stratification is shallower than wind-driven trapping depth. In these cases, H is set by the MLD associated with salinity stratification (the initial MLD due to salinity stratification does not change much during the GOTM simulation period), and the influence of surface cooling and wind-driven mixing is confined to the salinity-stratified mixed layer rather than the deeper wind-driven mixing scale.

Building on equation 1, we conduct four distinct cases of parameter space explorations by adjusting the idealized surface forcing based on the parameters mentioned in Table 1. In each parameter space exploration case, GOTM simulations are forced for 30-day runs with diurnally varying solar radiation peaking at Q_{SWR}^{peak} (based on Renner et al., 2019) and constant cooling components of heat fluxes (Q_{cool}, Figure 5d). This results in a daily mean net heat flux value of $\overline{Q_{net}}$ as mentioned in Table 1. Jerlov-I optical profile is used for all the cases, except case-4, which utilizes an optical profile observed in the NBoB during a 2019 field campaign (Figure 5c, see Kerhalkar et al., 2025b and Schlosser et al., 2025). We vary the initial MLD (2-15 m), ΔS_b (0-1 $\mathrm{g\,kg^{-1}}$) and wind speeds (3-6 $\mathrm{m\,s^{-1}}$) to explore the parameter space. We initially present the results for wind speeds of 5 $\mathrm{m\,s^{-1}}$ (trapping depth is estimated to be 13.4 m based on the formulation of Fairall et al., 1996b).

Table 1. Summary of Forcing Parameters and Optical Profiles for Idealized Cases.

Cases	$Q_{\mathrm{SWR}}^{\mathrm{peak}}$ $(\mathrm{W\,m^{-2}})$	Q_{cool} $(\mathrm{W\,m^{-2}})$	$\overline{Q_{net}}$ $(\mathrm{W\,m^{-2}})$	**Optics**
Case-1	1000	175	123	Jerlov-I
Case-2	1000	148	150	Jerlov-I
Case-3	1095	175	150	Jerlov-I
Case-4	1000	148	150	Observed

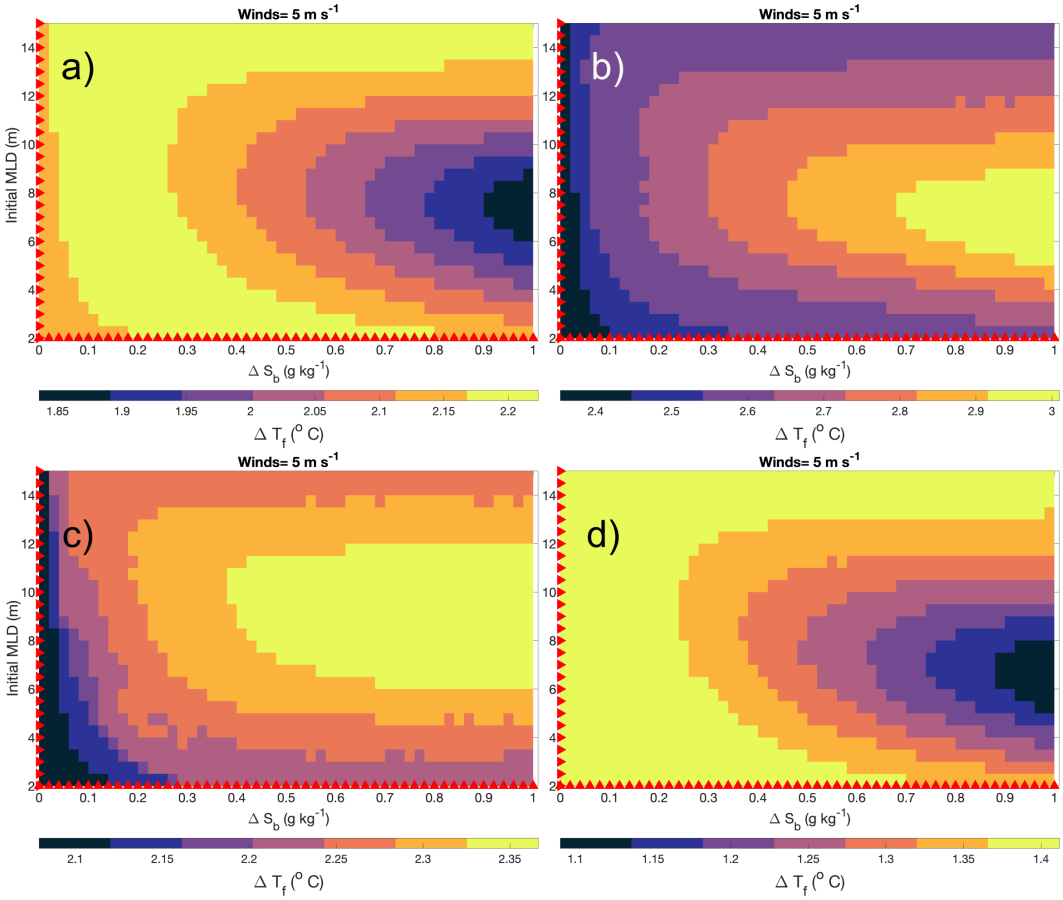

Figure 9. (a) ΔT_f over a 30-day period as a function of ΔS_b (x-axis) and initial MLD (y-axis) for a diurnally varying clear sky day with wind speed of 5 $\mathrm{m\,s^{-1}}$ for case-1. (b)-(d) is same as (a) for cases-2, 3, 4 respectively (Table 1). The red markers at axes indicate the different parameters for which the simulations are performed.

Case-1 shows that salinity-stratified scenarios yield a lower ΔT_f than non-stratified cases by approximately 0.35 °C (Figure 9a), primarily due to enhanced vertical heat flux divergence in the stratified scenarios. The impact of salinity stratification is largest for initial MLDs between 6–10 m, where the difference in vertical heat flux divergence (and hence ΔT_f, equation 1) between stratified and unstratified cases is maximized. This is as a result of difference in both H as well as $F(H).Q_{SWR}$ term in equation 1. For initial MLDs shallower than 6 m, the stratified effective mixed layer depth is much shallower than the wind-driven trapping depth in unstratified cases. Hence, the shallow mixed layer confines both the absorbed heat and the depth over which vertical heat flux divergence occurs, reducing the resulting ΔT_f contrast between stratified and unstratified scenarios. For initial MLDs deeper than 10 m, the contrast in vertical heat flux divergence between stratified and unstratified cases is smaller, as the effective MLD in stratified cases (set by the initial salinity profile) approaches the wind-driven trapping depth of the unstratified cases. This is consistent with the SEAS case (Figure 8a), where enhanced stratification suppresses surface warming.

In contrast, results from case-2 (where the $\overline{Q_{net}}$ is increased from case-1 by reducing Q_{cool}) reveal that ΔT_f increases as the ΔS_b increases (Figure 9b) by about 0.6 °C. Increasing $\overline{Q_{net}}$ provides more heat at the surface. So in stratified cases where H is confined to a comparatively shallow layer, this confinement reduces vertical heat flux divergence relative to unstratified cases, allowing more heat to be retained in the mixed layer and producing a larger ΔT_f. For initial MLDs between 5–8 m, the difference in vertical heat flux divergence between stratified and unstratified cases is maximized. For shallower initial MLDs, the stratified effective mixed layer (H) remains very shallow compared to the wind-driven trapping depth in unstratified cases, limiting the contrast in ΔT_f. For deeper initial MLDs, the effective MLD in stratified cases approaches the wind-driven trapping depth, making the vertical distribution of $F(H)\cdot Q_{SWR}$ similar and reducing the ΔT_f contrast. This impact of ΔS_b in this case is similar to the NBoB case (Figure 8b), thereby highlighting the role of $\overline{Q_{net}}$ in causing such contrasting effects of ΔS_b on ΔT_f.

Case-3 of the parameter space exploration further justifies the role of $\overline{Q_{net}}$. This case utilizes the Q_{cool} from case-1 with the $\overline{Q_{net}}$ of case-2 (achieved by increasing Q_{SWR}). Results mirror those of case-2 in trend, though absolute ΔT_f values differ (Figure 9c). This difference occurs because the simultaneous increase in both Q_{SWR} and Q_{cool} mod-

ifies the vertical heat flux divergence. Although more shortwave radiation is available at the surface, the larger cooling offsets part of this increase. Consequently, the vertical heat flux divergence difference between stratified and unstratified scenarios is somewhat smaller in case-3 compared to case-2, reducing the ΔT_f enhancement due to salinity stratification. The depth-dependent impact of ΔS_b on ΔT_f in this case is consistent with case-2 as well.

We conduct an additional parameter space exploration (case-4) where the water's optical properties are modified to allow deeper penetration of SWR (Figure 5c) while keeping all other surface forcing conditions similar to case-2. Comparison of results from case-4 and case-2 reveal that merely altering the optical properties leads to contrasting impacts of ΔS_b on ΔT_f. In case-4, salinity-stratified case warms less than non-salinity-stratified case by about 0.3°C (Figure 9d). This occurs because deeper penetration of SWR reduces the $\mathrm{F(H).Q_{SWR}}$ term (equation 1), thereby increasing the vertical heat flux divergence for the stratified case. These idealized cases highlight the importance of surface heat fluxes and water's optical properties in driving the contrasting effects of ΔS_b on ΔT_f.

Next, we investigate the impact of varying wind speeds on our simulations. As mentioned earlier, wind drives unrestricted vertical mixing in non-salinity-stratified scenarios . On the other hand, mixing is suppressed for salinity-stratified cases and wind mainly controls the entrainment across the stratified layer (e.g., Dewey & Moum, 1990). For simplicity, we intentionally exclude the effect of changing wind speeds on Q_{cool} in these idealized cases, although this is considered later and the results are qualitatively similar.

For idealized scenarios where ΔT_f increases with increasing ΔS_b (such as case-2), the influence of salinity stratification is more pronounced at higher wind speeds than at lower wind speeds (Figure 10). This occurs because higher wind speeds enhance entrainment across the stratified interface in salinity-stratified cases, while in non-salinity-stratified scenarios they promote deeper vertical mixing throughout the water column, thereby intensifying the ΔT_f contrast. Conversely, at lower wind speeds, vertical mixing in both salinity-stratified and non-salinity-stratified cases occurs over similar depth scales (since the wind-driven trapping depth scale for 3 $\mathrm{m\,s^{-1}}$ wind forcing is nearly 5.4 m, see Fairall et al., 1996b), leading to only small differences in vertical heat flux divergence and, consequently, a reduced contrast in the corresponding ΔT_f values.

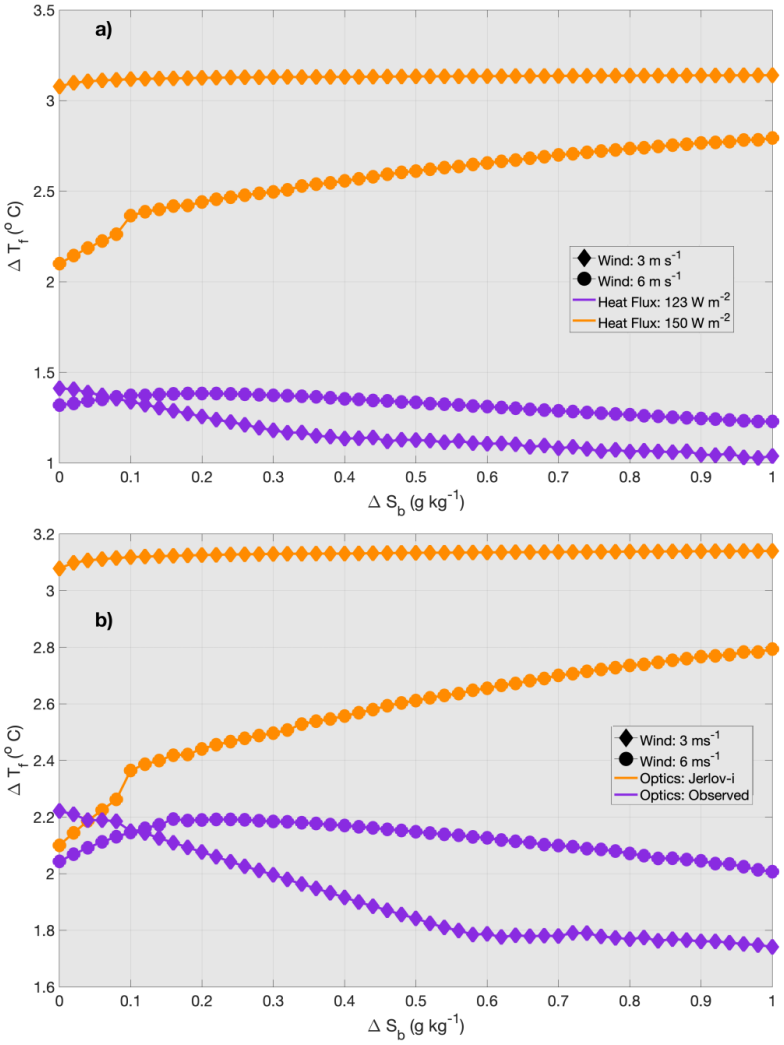

Figure 10. (a) ΔT_f over a 30-day period as a function of ΔS_b (x-axis) for an initial MLD=8 m for a diurnally varying clear sky day with daily $\overline{Q_{net}}$ of 123 (purple, Case-1) and 150 W m^{-2} (orange, Case-2), different wind speed scenarios (diamond and circle markers for 3 m s^{-1} and 6 m s^{-1} winds respectively). (b) is the same as (a) but for a daily $\overline{Q_{net}}$ of 150 W m^{-2} and different optical profiles (Jerlov-I in orange and observed optical profile in purple respectively, Case-2 and 4).

However, for idealized scenarios in which ΔT_f decreases with increasing ΔS_b (cases 1 and 4), the influence of salinity stratification is more pronounced at lower wind speeds (Figure 10). Under weak wind forcing, stratification more effectively suppresses entrainment, limiting vertical exchange and reducing the net warming within the mixed layer. As wind speed increases, this contrast weakens and the response of ΔT_f to increasing

ΔS_b becomes less systematic. In some cases, ΔT_f initially increases with ΔS_b before decreasing at larger stratification. This non-monotonic behavior reflects the competing roles of stratification and wind-driven entrainment, and highlights that the wind-speed dependence of ΔT_f cannot be described solely by the surface heat budget in equation 1, but instead involves additional dynamical effects associated with entrainment.

6 Crossover Heat Flux: Quantifying the ΔT_f vs ΔS_b Regime Shift

As previously discussed, the dependence of ΔT_f on ΔS_b is sensitive to $\overline{Q_{net}}$ (through diurnally varying Q_{SWR} and Q_{cool}), the optical properties of water as well as the effective mixed layer depth (H). To mathematically identify the $\overline{Q_{net}}$ value at which this qualitative shift occurs, we derive the crossover heat flux (Q_{cross}), defined as the $\overline{Q_{net}}$ value where the ΔT_f is equal for the non-salinity stratified and the salinity-stratified scenarios. Physically, Q_{cross} marks the threshold daily-mean net surface heat flux beyond which daytime heat absorption exceeds nighttime losses more effectively in stratified scenarios than in unstratified scenarios, leading to greater relative warming. When $\overline{Q_{net}}$ exceeds Q_{cross}, the salinity-stratified scenario exhibits higher ΔT_f. Conversely, when $\overline{Q_{net}}$ does not exceed Q_{cross}, the salinity-stratified scenario exhibits lower ΔT_f. The derivation of Q_{cross} utilizes the simple 1-D heat budget equation described in equation 1.

$$\Delta T_f^{str} - \Delta T_f^{unstr} = \frac{F(H_{str}).\overline{Q_{SWR}} - \overline{Q_{cool}}}{\rho c_p H_{str}} - \frac{F(H_{unstr}).\overline{Q_{SWR}} - \overline{Q_{cool}}}{\rho c_p H_{unstr}} \tag{2}$$

The integral in equation 1 is replaced by daily mean (overbar) quantities for SWR (Q_{SWR}) and cooling heat fluxes (Q_{cool}). We assume that the heat flux quantities are identical in both the non-salinity-stratified (labeled "unstr") and salinity-stratified scenarios (labeled "str"). The H_{str} and H_{unstr} represent the effective depths controlled by the shallow salinity-stratification and deeper temperature-stratification/wind mixing respectively. Equating equation 2 to zero as to get $\Delta T_f^{str} = \Delta T_f^{unstr}$, yields a daily mean cooling heat flux expression as:

$$\overline{Q_{cool}} = \left[\frac{F(H_{str}).H_{unstr} - F(H_{unstr}).H_{str}}{H_{unstr} - H_{str}}\right] \overline{Q_{SWR}} \tag{3}$$

Using the expression for $\overline{Q_{cool}}$ in equation 3, we derive an expression for Q_{cross} as $\overline{Q_{SWR}} - \overline{Q_{cool}}$ (or the $\overline{Q_{net}}$ value where $\Delta T_f^{str} = \Delta T_f^{unstr}$), where H^* as the ratio between H_{unstr} and H_{str}:

$$Q_{cross} = \left[\frac{H^*[1 - F(H_{str})] - [1 - F(H_{unstr})]}{H^* - 1}\right] \overline{Q_{SWR}} \tag{4}$$

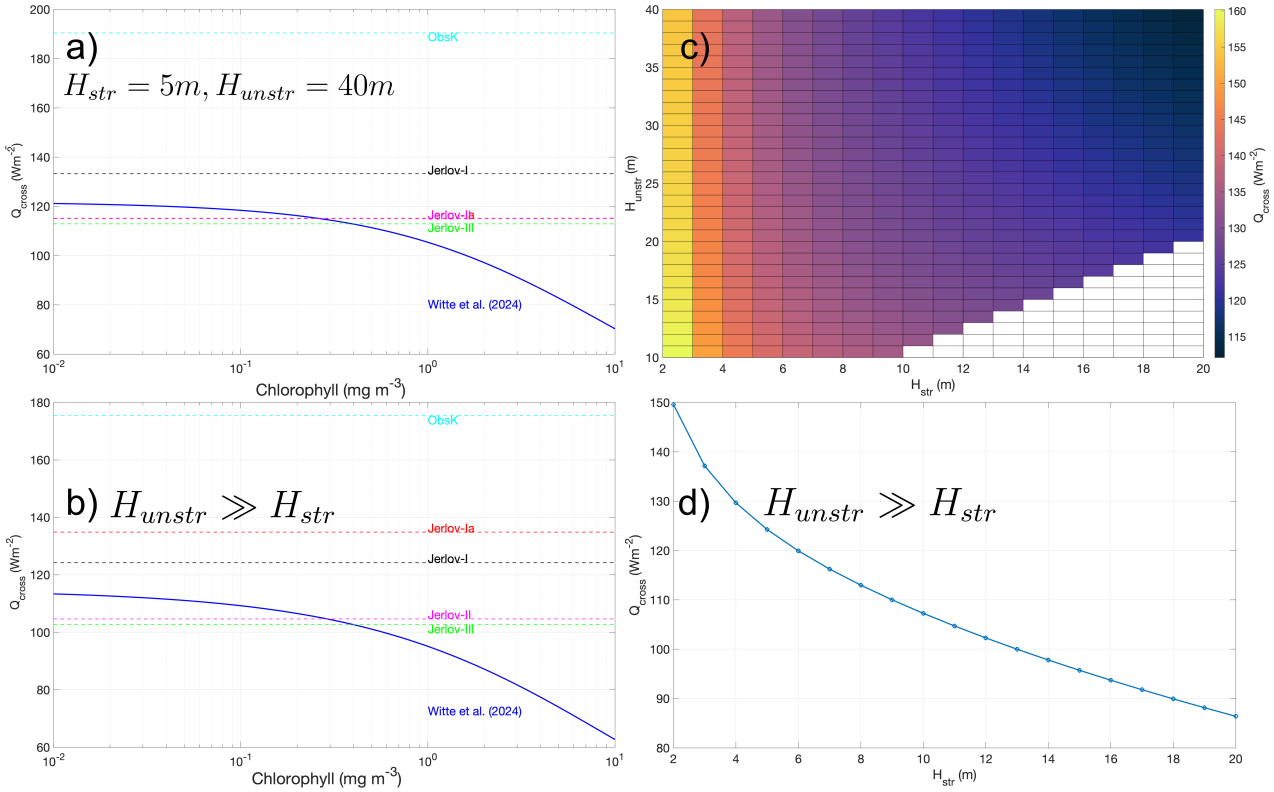

Figure 11. (a) Q_{cross} (in blue) as a function of Chlorophyll (log-scale in x-axis) based on optical profiles from Witte et al. (2024) for H_{str}=5 m and H_{unstr}= 40 m. Colored horizontal lines represent Q_{cross} corresponding to different Jerlov water types (as described in Paulson & Simpson, 1977), and to an observed optical profile in the Bay of Bengal (light blue, Schlosser et al., 2022). Black, red, magenta, and green lines indicate Jerlov types I, Ia, II, and III, respectively. (b) is same as (a) for the special case where H_{unstr} is much larger than H_{str} (equation 5). (c) Q_{cross} as a function of H_{str} (x-axis) and H_{unstr} (y-axis) for Jerlov-I water type for a typical clear sky day in April (based on equation 4). (d) Q_{cross} as a function of H_{str} for Jerlov-I water type in the special case where H_{unstr} is much larger than H_{str} (equation 5).

We use equation 4 for a representative case in this study (H_{str}= 5 m and H_{unstr}= 40 m) to estimate Q_{cross} using both theoretical optical profiles (Paulson & Simpson, 1977) and observed optical profiles from the NBoB (Schlosser et al., 2022; Kerhalkar et al., 2025b). We also incorporate chlorophyll-dependent optical profile parameterizations based on Witte et al. (2024) to examine the influence of chlorophyll on Q_{cross}.

Our results show that for a typical clear sky day in April, Q_{cross} values derived using theoretical optical profiles range between 115 to 135 W m^{-2} (Figure 11a). Q_{cross} val-

ues for Jerlov-I water type is calculated to be around 135 $\mathrm{W\,m^{-2}}$, compared to about 190 $\mathrm{W\,m^{-2}}$ when derived for the NBoB observed optical profiles. This higher Q_{cross} value aligns with the NBoB observations of waters clearer than Jerlov-I at times (pers comm: Tamara Schlosser). Enhanced water clarity promotes deeper SWR penetration, which accounts for the higher derived Q_{cross}. Q_{cross} for chlorophyll-dependent optical profiles reveals a monotonic decrease with a nonlinear decay as chlorophyll increases, with values ranging from 75 to 120 $\mathrm{W\,m^{-2}}$ (Figure 11a). For optical profiles corresponding to murkier waters (i.e., higher chlorophyll concentrations), Q_{cross} values are lower due to increased absorption of SWR within the MLD. Varying the values of H_{str} and H_{unstr} for Jerlov-I water type reveals Q_{cross} values ranging from 110 to 160 $\mathrm{W\,m^{-2}}$ (Figure 11c). Highest Q_{cross} values occur for shallower H_{str}. Conversely, Q_{cross} reaches its minimum when both H_{str} and H_{unstr} are deep.

A special limiting case occurs assuming that $H_{unstr} \gg H_{str}$. This represents a well-mixed scenario with an effectively infinitely deep mixed layer and pycnocline, when equation 4 simplifies to:

$$Q_{cross} = [1 - F(H_{str})]\,\overline{Q_{SWR}} \tag{5}$$

The Q_{cross} values estimated using the simplified case of an infinitely deep unstratified mixed layer ($H_{\mathrm{unstr}} \gg H_{\mathrm{str}}$; equation 5) closely align with those from the full formulation discussed earlier (Figure 11b, 11d, Equation 4).

To verify the validity of the Q_{cross} formulation in Equation 4, we conducted a suite of 1-D simulations with varying stratified mixed layer depths (H_{str}), daily mean net heat flux ($\overline{Q_{net}}$), and wind speeds. The results show that Q_{cross} estimates from the simulations closely match the theoretical values from Equation 4 under low-wind conditions (Figure 12a). For 6 $\mathrm{m\,s^{-1}}$ wind speeds, however, the model-derived Q_{cross} deviates from the theoretical formulation by about 5–10 $\mathrm{W\,m^{-2}}$ (Figure 12b), highlighting the weaker influence of entrainment on the Q_{cross} formulation in Equation 4. Importantly, the overall trend of Q_{cross} from model simulations is consistent with the theoretical estimates.

The theoretical framework developed in this section not only highlights the unique roles of the initial upper ocean structure, water's optical properties, and surface heat fluxes in characterizing SST evolution and its spatial variability, but also offers a quantitative basis for interpreting how diurnal atmospheric processes imprint onto the ocean surface

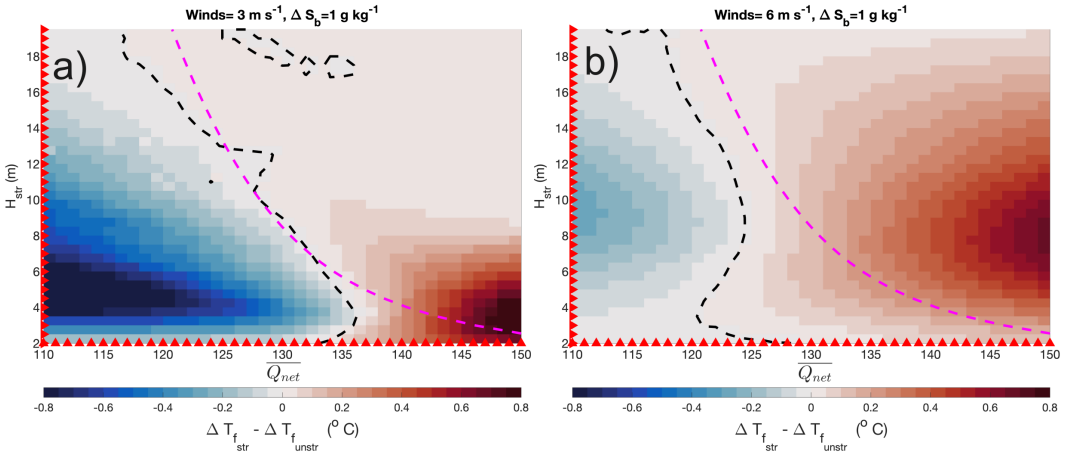

Figure 12. (a) Difference in ΔT_f over a 30-day period between a salinity-stratified scenario (varying H_{str}, $\Delta S_b = 1\ \mathrm{g\,kg^{-1}}$) and an unstratified (or deeper-stratified) scenario ($H_{unstr} = 20$ m, $\Delta S_b = 1\ \mathrm{g\,kg^{-1}}$) as a function of daily mean net heat flux ($\overline{Q_{net}}$, x-axis) and H_{str} (y-axis) for Jerlov-I water type and wind speed of 3 $\mathrm{m\,s^{-1}}$. The black dashed line indicates the contour where the difference in ΔT_f is zero (i.e., Q_{cross} from GOTM simulations), while the magenta dashed line indicates Q_{cross} from Equation 4. Red markers on the axes denote the parameter values used in the simulations. (b) Same as (a), except with wind speed of 6 $\mathrm{m\,s^{-1}}$.

and accumulate into SST variability on longer time scales under varying stratification conditions.

7 Discussion

The results presented here highlight significant differences of O(1°C) in foundational SST warming (ΔT_f) across intra-seasonal timescales and over mesoscale and smaller lengths in the Northern Indian Ocean. These variations reflect spatial differences in surface heat fluxes, wind speed, salinity stratification, and water optical properties, all of which are observed to vary across these scales (e.g., Moshonkin & Harenduprakash, 1991; Song et al., 2022; Nuijens et al., 2023; Shroyer et al., 2016; Kerhalkar et al., 2025b; McKie et al., 2024; Pimentel et al., 2019). The lateral gradients in SST evolution arise from the interplay between fast-moving atmospheric systems, which drive transient variability in winds and surface fluxes, and much slower-evolving salinity features. Whereas wind-driven variability produces short-lived flux gradients as weather systems pass, the persistence

of salinity-driven stratification generates more enduring lateral contrasts in SST and associated air–sea fluxes across a range of spatial and temporal scales.

Idealized 1-D simulations forced with surface heat fluxes from in-situ moorings reveal that O(0.5°C) of the ΔT_f differences are attributable to the role of salinity stratification. Both stratified and unstratified scenarios warm in an absolute sense but differ in relative heating. These simulations further show that when daily mean net heat flux ($\overline{Q_{net}}$) exceeds a critical threshold (Q_{cross}), the stratified conditions lead to stronger warming compared to unstratified cases. The opposite is true for daily mean net heat fluxes below Q_{cross}. This response contrasts with the influence of salinity stratification on diurnal SST amplitudes, which consistently increase by about 0.07-0.15 °C under stratified conditions regardless of the heat flux regime (Kerhalkar et al., 2025b). The ΔT_f differences described above also suggest a possible feedback on the surface heat fluxes (particularly the cooling component of heat fluxes) driven by salinity stratification, which is not accounted for in the above simulations. To explore this, we use 1-D GOTM in a one-way coupled configuration such that the model is forced with observed meteorological conditions. The model computes the fluxes internally based on the COARE algorithm (Fairall et al., 1996a) using the model-derived SSTs. Results from these coupled simulations confirm that the influence of salinity stratification on ΔT_f differences persists (Figure S4) and reveal that the resulting impact on surface heat fluxes are O(10 $\mathrm{W\,m^{-2}}$) (Figure S5).

While the physical mechanisms discussed here are robust, the magnitude of ΔT_f over intra-seasonal timescales is sensitive to vertical entrainment (e.g., Seager et al., 1988). Recent studies have shown that entrainment beneath the mixed layer and hence the SST is sensitive to the choice of the 1-D model/turbulence closure scheme (Johnson et al., 2023b). Because entrainment could potentially modify the mixed layer depth, Q_{cross} may be sensitive to the chosen mixing scheme and the temporal evolution of mixed layer (which is not captured as stratification in the GOTM does not change much during the simulation period). The use of the Mellor-Yamada mixing scheme within the GOTM framework (Mellor & Yamada, 1982), instead of the k-ϵ scheme, yielded similar O(0.5°C) of the ΔT_f differences due to salinity stratification differences (Figure S6). Similarly, the Q_{cross} derived using Mellor-Yamada mixing scheme is comparable to that obtained from k-ϵ mixing scheme and agrees well with theoretical formulations (Figure S7).

Our discussions of Q_{cross} in this study are currently limited to clear sky conditions, reflecting typical conditions during the spring intermonsoon season in the NIO (Figure 2). However, the application of the derived formulation (equation 4 and 5) indicates that the values of Q_{cross} in the North Indian Ocean can range between 50-150 $\mathrm{W\,m^{-2}}$ depending on the time of the year, cloud cover conditions in the region for Bay of Bengal and Arabian Sea (Figure S8) H_{str} and H_{unstr} of 5 and 40 m respectively and Jerlov-I water type (Paulson & Simpson, 1977). Comparison of Q_{cross} with observed daily mean net heat flux ($\overline{Q_{net}}$) at AD08 and ASIRI moorings shows that the latter exceeds Q_{cross} 11.6% of the time in SEAS (AD08) and 21.4% at the ASIRI mooring in NBoB over the observation period (Figure S8). During February–May (mini–warm pool formation), these probabilities are 10.8% at SEAS (AD08) and 38% at NBoB (ASIRI). Allowing for a 5 $\mathrm{W\,m^{-2}}$ uncertainty in Q_{cross} due to vertical entrainment (see Section 6) increases the exceedance frequencies to 15.7% and 26% for SEAS and NBoB respectively (period average), and to 15.8% and 48% during the mini–warm pool months in SEAS and NBoB respectively (Figure S8). Using fluxes from the MERRA-2 reanalysis for 2015 (Global Modeling and Assimilation Office (GMAO), 2015) in the Northern Indian Ocean, we find that the probabilities of $\overline{Q_{net}}$ exceeding Q_{cross} (Figure S9) are similar to those reported from in-situ observations, with clear spatial variability in the probabilities.

Building on the earlier discussion of Q_{cross}, these results imply that in regions with prominent salinity fronts, differential ΔT_f across the front is expected. This could either enhance the density across the front or cause density compensation depending on the value of surface heat fluxes. However, these dynamics are likely to be influenced by unresolved processes such as mesoscale advection and submesoscale frontal activity, which are not represented in our 1-D framework (e.g., Buckley et al., 2020; Jaeger & Mahadevan, 2018; Kerhalkar et al., 2025a).

While freshwater fronts in the Indian Ocean are primarily driven by riverine input, the freshwater is typically turbid. Hence, the impacts of such fronts should ideally be studied as a coupled effect of salinity and optical properties. In this study, however, we do not consider this coupling, in order to highlight and isolate the role of salinity stratification. Additionally, the optical profile from NBoB used in this study to illustrate the role of optics (case-4 in Section-5 of this paper) is based on observations in the Bay of Bengal during July 2019 (i.e. the Monsoon season) and does not specifically represent

the water's optical properties during the spring intermonsoon season, nor the turbid conditions associated with riverine input.

The resulting differences in SST evolution and upper-ocean heat distribution, driven by both salinity stratification and optical properties, are particularly relevant for the North Indian Ocean. Given the tight coupling between marine atmospheric boundary layer (MABL) and the ocean boundary layer (e.g., Seo et al., 2023; Sullivan et al., 2020, 2021), SST fronts introduced as a result can influence atmospheric convection, generate secondary circulations, and modulate other MABL characteristics on intra-seasonal timescales (Skyllingstad et al., 2007). The resulting MABL adjustments subsequently modulate SST variability and upper ocean thermal structure. Such variability during the pre-monsoon heating periods examined here is critical for driving key air-sea interaction processes, including tropical cyclone development (Vinayachandran et al., 2007), and for affecting monsoon forecasts across sub-seasonal to seasonal timescales (Krishnamurti et al., 2007). Understanding these processes requires close examination of interactions between the ocean and atmospheric boundary layers, highlighting the importance of accounting for fine-scale biophysical interactions in sub-seasonal and seasonal forecasting.

8 Conclusion

The northern Indian Ocean experiences strong upper ocean heating during the spring intermonsoon season that precedes the monsoon (Figure 1). Over 90% of the days during this period show a net heat gain by the ocean (Figure 2). However, remote sensing observations reveal that this heating is spatially heterogeneous, with intra-seasonal (15–60 day) differences in T_f warming rates of O(1°C) across mesoscale and smaller lengths ($<$ 100 km). These variations are accompanied by lateral differences in surface wind speeds and salinity of O(2 $\mathrm{m\,s^{-1}}$) and O(2 $\mathrm{g\,kg^{-1}}$) respectively (Figure 3). Argo float profiles further indicate variability in mixed layer depths of O(25 m) across the region. All of the above mentioned factors can contribute to the spatial variability in the surface heating rates as well as air-sea heat flux values on intra-seasonal timescales.

To evaluate the role of salinity stratification in modulating these gradients, we conducted a suite of 1-D simulations. Simulations forced with realistic surface fluxes from mooring records in the northern Indian Ocean, reveal 0.2-0.5°C differences in ΔT_f change over 14-21 days due to salinity stratification differences (Figure 6- 8). This variability

is evident only for cases with shallow initial mixed layers (< 14 m). Interestingly, the role of salinity stratification on the ΔT_f is contrasting; for the Arabian Sea scenario, the stratified case warms comparatively less than the unstratified case (Figure 7, 8a), whereas for the Bay of Bengal, the stratified case have higher or lower warming rates than the unstratified case at times (Figure 6, 8b, S1, S2, S3). To further investigate this contrast, we conduct idealized simulations with constant wind speeds, diurnally varying shortwave radiation (for a clear-sky day scenario), constant cooling components of heat fluxes and optical properties of water (Figure 5d, Table 1). Our results demonstrate that relative warming in stratified case when compared to unstratified case is sensitive to the net surface heat flux and optical properties of water. Under higher daily mean net heat flux and more turbid scenarios, the stratified cases warm comparatively more than the unstratified case (Figure 9, 10). This suggests that in regions with strong salinity fronts, elevated heat fluxes and turbidity can enhance density contrasts across the front, which is more pronounced under higher wind speeds. In contrast, the initial salinity front may become partially density-compensated due to comparitively reduced warming in the stratified case than unstratified during lower daily mean net heat flux or clearer water conditions. This particular effect is pronounced under lower wind speeds.

Finally, we derive an analytical expression for crossover heat flux (Q_{cross}), defined as the heat flux at which stratified and unstratified scenarios have an equal ΔT_f. When the daily mean net heat flux values exceeds Q_{cross}, presence of salinity stratification causes comparatively more surface warming than in unstratified cases. Q_{cross} is found to be a function of water's optical properties, inital mixed layer depth for stratified and unstratified cases and the daily mean shortwave radiation. For a representative case of mixed layer depths of 5 m and 40 meter for stratified and unstratified cases respectively under clear sky conditions with peak shortwave radiation of 1000 $\mathrm{W\,m^{-2}}$, Q_{cross} vary between 110 $\mathrm{W\,m^{-2}}$ (for Jerlov-III water type) and 135 $\mathrm{W\,m^{-2}}$ (for Jerlov-I water type, Figure 11a, 11c). Assuming an infinitely deep mixed layer for the unstratfied case, the above Q_{cross} values change to 103 $\mathrm{W\,m^{-2}}$ and 125 $\mathrm{W\,m^{-2}}$ respectively (Figure 11b, 11d). The theoretical formulation of Q_{cross} is supported by 1-D model simulations, showing close agreement under low-wind conditions and consistent overall trends across turbulence closure schemes (Figure S6,S7). Additionally, the crossover flux values have a strong dependency on the optical absorption properties. The range of Q_{cross} values and the observed daily mean net heat fluxes helps to clarify the role of salinity stratification on dif-

ferent outcomes of surface warming observed in our simulation results, underscoring the unique role of bio-physical coupling in upper ocean heating. The differences in SST evolution and upper ocean heat distribution due to the role of salinity stratification and optical properties highlighted in this study could have potential impacts on tropical cyclone and monsoon forecasts.

Open Research Section

The NIOT mooring data are available at: `http://do.incois.gov.in/` and were obtained through a request to the Indian National Centre for Ocean Information Services (INCOIS). The WHOI mooring data from 2015 can be accessed at `http://uop.whoi.edu/projects/Bengal/QCData.html`. SMAP and OISST satellite data were obtained from `www.remss.com`. ARGO data were obtained using ARGOPy python library (Maze & Balem, 2020). Simulations were performed using version 6.0 of the General Ocean Turbulence Model (GOTM), available at `https://gotm.net/portfolio/`.

Acknowledgments

The authors would like to thank US Office of Naval Research for their support to the ASIRI, MISO-BoB and EKAMSAT Department Research Initiative. S.Kerhalkar and A.Tandon were supported by N00014-17-1-2355, N00014-18-1-2799, N00014-19-1-2410 and N00014-23-1-2054, while J.MacKinnon was supported by N00014-23-1-2056. S. Kerhalkar was additionally supported under grant N00014-24-1-2570 (PI: Hyodae Seo), and A. Tandon under grant N00014-23-1-2473. S.Kerhalkar would like to thank the Associate Provost's office, University of Massachusetts Dartmouth for their support through the Distinguished Doctoral Fellowship. The authors are thankful to Alex Kinsella, Tom Farrar, Tamara Schlosser, Leah Johnson, Kenneth Hughes, Steven Lohrenz, Miles Sundermeyer, Elizabeth Thompson and Debasis Sengupta for their stimulating discussions on various aspects of this work, and to Debarshi Sarkar for assistance with curating data from the NIOT moorings. The authors would like to express their sincere gratitude to Deepak Cherian, an anonymous reviewer and the editor, Bieito Fernández Castro for their constructive suggestions, which greatly enhanced the quality and clarity of this manuscript.

References

Balaguru, K., Chang, P., Saravanan, R., Leung, L. R., Xu, Z., Li, M., & Hsieh,

667 J.-S. (2012, September). Ocean barrier layers' effect on tropical cyclone
668 intensification. *Proceedings of the National Academy of Sciences*, *109*(36),
669 14343–14347. Retrieved 2025-05-31, from https://www.pnas.org/doi/abs/
670 10.1073/pnas.1201364109 (Publisher: Proceedings of the National Academy
671 of Sciences) doi: 10.1073/pnas.1201364109

672 Beal, L. M., Vialard, J., Roxy, M. K., Li, J., Andres, M., Annamalai, H., ... Par-
673 vathi, V. (2020). A Road Map to IndOOS-2: Better Observations of the
674 Rapidly Warming Indian Ocean. *Bulletin of the American Meteorological Soci-*
675 *ety*, *101*(11), E1891–E1913. Retrieved from https://journals.ametsoc.org/
676 view/journals/bams/101/11/bamsD190209.xml (Publisher: American Mete-
677 orological Society Place: Boston MA, USA) doi: 10.1175/BAMS-D-19-0209.1

678 Brown, M. E., Escobar, V., Moran, S., Entekhabi, D., O'Neill, P. E., Njoku, E. G.,
679 ... Entin, J. K. (2013, August). NASA's Soil Moisture Active Passive
680 (SMAP) Mission and Opportunities for Applications Users. Retrieved 2025-
681 06-03, from https://journals.ametsoc.org/view/journals/bams/94/8/
682 bams-d-11-00049.1.xml (Section: Bulletin of the American Meteorological
683 Society) doi: 10.1175/BAMS-D-11-00049.1

684 Buckley, J. M., Mingels, B., & Tandon, A. (2020, February). The impact of lateral
685 advection on SST and SSS in the northern Bay of Bengal during 2015. *Deep*
686 *Sea Research Part II: Topical Studies in Oceanography*, *172*, 104653. Retrieved
687 2025-05-28, from https://www.sciencedirect.com/science/article/pii/
688 S0967064519300906 doi: 10.1016/j.dsr2.2019.104653

689 Burchard, H., Bolding, K., Rippeth, T. P., Stips, A., Simpson, J. H., & Sündermann,
690 J. (2002, June). Microstructure of turbulence in the northern North
691 Sea: a comparative study of observations and model simulations. *Jour-*
692 *nal of Sea Research*, *47*(3-4), 223–238. (Publisher: Elsevier) doi: 10.1016/
693 S1385-1101(02)00126-0

694 Burchard, H., Bolding, K., & Villarreal, M. R. (1999). *GOTM, a general ocean tur-*
695 *bulence model: theory, implementation and test cases.* Space Applications In-
696 stitute.

697 Canuto, V. M., Howard, A., Cheng, Y., & Dubovikov, M. S. (2001). Ocean tur-
698 bulence. Part {I}: One-point closure model—Momentum and heat vertical
699 diffusivities. *Journal of Physical Oceanography*, *31*(6), 1413–1426. Re-

trieved from https://doi.org/10.1175/1520-0485(2001)031%3C1413:OTPIOP%3E2.0.CO;2

Chaudhuri, D., Sengupta, D., D'Asaro, E., & Shivaprasad, S. (2021). Trapping of Wind Momentum in a Salinity-Stratified Ocean. *Journal of Geophysical Research: Oceans*, *126*(12), e2021JC017770. Retrieved 2025-05-31, from https://onlinelibrary.wiley.com/doi/abs/10.1029/2021JC017770 (_eprint: https://onlinelibrary.wiley.com/doi/pdf/10.1029/2021JC017770) doi: 10.1029/2021JC017770

Chaudhuri, D., Sengupta, D., D'Asaro, E., Venkatesan, R., & Ravichandran, M. (2019). Response of the salinity-stratified Bay of Bengal to cyclone Phailin. *Journal of Physical Oceanography*, *49*(5), 1121–1140.

Clayson, C. A., & Weitlich, D. (2007, January). Variability of Tropical Diurnal Sea Surface Temperature. Retrieved 2025-05-31, from https://journals.ametsoc.org/view/journals/clim/20/2/jcli3999.1.xml (Section: Journal of Climate) doi: 10.1175/JCLI3999.1

de Szoeke, S. P., Marke, T., & Brewer, W. A. (2021). Diurnal Ocean Surface Warming Drives Convective Turbulence and Clouds in the Atmosphere. *Geophysical Research Letters*, *48*(4). doi: 10.1029/2020GL091299

Dewey, R. K., & Moum, J. N. (1990). Enhancement of fronts by vertical mixing. *Journal of Geophysical Research*, *95*(C6), 9433. doi: 10.1029/jc095ic06p09433

Donlon, C., Robinson, I., Casey, K. S., Vazquez-Cuervo, J., Armstrong, E., Arino, O., ... others (2007). The global ocean data assimilation experiment high-resolution sea surface temperature pilot project. *Bulletin of the American Meteorological Society*, *88*(8), 1197–1214. (Publisher: American Meteorological Society)

Drushka, K., Asher, W. E., Ward, B., & Walesby, K. (2016). Understanding the formation and evolution of rain-formed fresh lenses at the ocean surface. *Journal of Geophysical Research: Oceans*, *121*(4), 2673–2689. Retrieved from https://doi.org/10.1002/2015JC011527 (Publisher: Wiley Online Library)

Echols, R., & Riser, S. C. (2020). The Impact of Barrier Layers on Arabian Sea Surface Temperature Variability. *Geophysical Research Letters*, *47*(3), e2019GL085290. Retrieved 2025-05-31, from https://onlinelibrary.wiley.com/doi/abs/10.1029/2019GL085290 (_eprint:

https://agupubs.onlinelibrary.wiley.com/doi/pdf/10.1029/2019GL085290) doi: 10.1029/2019GL085290

Edson, J. B., Jampana, V., Weller, R. A., Bigorre, S. P., Plueddemann, A. J., Fairall, C. W., ... Hersbach, H. (2013). On the exchange of momentum over the open ocean. *Journal of Physical Oceanography*, *43*(8), 1589–1610.

Fairall, C. W., Bradley, E. F., Godfrey, J. S., Wick, G. A., Edson, J. B., & Young, G. S. (1996b, January). Cool-skin and warm-layer effects on sea surface temperature. *Journal of Geophysical Research: Oceans*, *101*(C1), 1295–1308. Retrieved from `https://doi.org/10.1029/95JC03190` (Publisher: John Wiley & Sons, Ltd) doi: https://doi.org/10.1029/95JC03190

Fairall, C. W., Bradley, E. F., Hare, J. E., Grachev, A. A., & Edson, J. B. (2003). Bulk parameterization of air-sea fluxes: Updates and verification for the COARE algorithm. *Journal of Climate*, *16*(4), 571–591. doi: 10.1175/1520-0442(2003)016⟨0571:BPOASF⟩2.0.CO;2

Fairall, C. W., Bradley, E. F., Rogers, D. P., Edson, J. B., & Young, G. S. (1996a). Bulk parameterization of air-sea fluxes for tropical oceanglobal atmosphere coupled-ocean atmosphere response experiment. *Journal of Geophysical Research C: Oceans*, *101*(C2), 3747–3764. doi: 10.1029/95JC03205

Gadgil, S. (2003). The Indian monsoon and its variability. *Annual Review of Earth and Planetary Sciences*, *31*(1998), 429–467. doi: 10.1146/annurev.earth.31.100901.141251

Global Modeling and Assimilation Office (GMAO). (2015). *MERRA-2 tavg1_2d_lnd_nx: 2d,1-Hourly,Time-Averaged,Single-Level,Assimilation,Land Surface Diagnostics V5.12.4.* (Published: Greenbelt, MD, USA, Goddard Earth Sciences Data and Information Services Center (GES DISC)) doi: 10.5067/RKPHT8KC1Y1T

Hormann, V., Centurioni, L. R., & Gordon, A. L. (2019). Freshwater export pathways from the Bay of Bengal. *Deep-Sea Research Part II: Topical Studies in Oceanography*, *168*(September), 104645. Retrieved from `https://doi.org/10.1016/j.dsr2.2019.104645` (Publisher: Elsevier Ltd) doi: 10.1016/j.dsr2.2019.104645

Jaeger, G. S., & Mahadevan, A. (2018). Submesoscale-selective compensation of fronts in a salinity-stratified ocean. *Science Advances*, *4*(2). doi: 10.1126/

sciadv.1701504

Jarugula, S., Sengupta, D., Shroyer, E., & Papa, F. (2024). Mixing of Rain and River Water in the Bay of Bengal From Basin-Scale Freshwater Balance. *Geophysical Research Letters*, *51*(3), e2023GL106451. Retrieved 2025-05-31, from `https://onlinelibrary.wiley.com/doi/abs/10.1029/2023GL106451` (_eprint: https://agupubs.onlinelibrary.wiley.com/doi/pdf/10.1029/2023GL106451) doi: 10.1029/2023GL106451

Johnson, L., Fox-Kemper, B., Li, Q., Pham, H. T., & Sarkar, S. (2023a). A Finite-Time Ensemble Method for Mixed Layer Model Comparison. *Journal of Physical Oceanography*.

Johnson, L., Fox-Kemper, B., Li, Q., Pham, H. T., & Sarkar, S. (2023b). A Finite-Time Ensemble Method for Mixed Layer Model Comparison. *Journal of Physical Oceanography*, *53*(9), 2211–2230. doi: 10.1175/JPO-D-22-0107.1

Joseph, K. J., Tandon, A., Venkatesan, R., Farrar, J. T., & Weller, R. A. (2022). Longwave Radiation Corrections for the OMNI Buoy Network. *Journal of Atmospheric and Oceanic Technology*, *39*(2), 271–282. doi: 10.1175/JTECH-D-21-0069.1

Kerhalkar, S., Kannad, A., Kinsella, A., Tandon, A., Sprintall, J., & Lee, C. M. (2025a). Monsoon-Frontal Interactions Drive Cyclone Biparjoy's Wake Recovery in the Arabian Sea. *Geophysical Research Letters*, *52*(4). doi: 10.1029/2024GL112413

Kerhalkar, S., Tandon, A., Farrar, J. T., MacKinnon, J. A., Schlosser, T. L., Johnson, L., ... Centurioni, L. R. (2025b). Modulation of Diurnal SST and Diurnal Warm Layer Variability by Salinity-Driven Stratification in the Bay of Bengal. *Journal of Physical Oceanography*, e250134.

Krishnamurti, T. N., Chakraborty, A., Krishnamurti, R., Dewar, W. K., & Clayson, C. A. (2007). Passage of intraseasonal waves in the subsurface oceans. *Geophysical Research Letters*, *34*(14), 1–5. doi: 10.1029/2007GL030496

Mahadevan, A., Jaeger, G. S., Freilich, M., Omand, M. M., Shroyer, E. L., & Sengupta, D. (2016, September). Freshwater in the Bay of Bengal. *Oceanography*, *29*(2), 72–81. Retrieved from `http://www.jstor.org/stable/24862671` (Publisher: Oceanography Society)

Maze, G., & Balem, K. (2020, September). argopy: A Python library for Argo ocean data analysis. *Journal of Open Source Software*, *5*(53), 2425. Retrieved 2025-06-03, from https://joss.theoj.org/papers/10.21105/joss.02425 doi: 10.21105/joss.02425

McKie, T., Lucas, A. J., & MacKinnon, J. (2024). Submesoscale Dynamics in the Bay of Bengal: Inversions and Instabilities. *Journal of Geophysical Research: Oceans*, *129*(3), e2023JC020563. Retrieved 2025-05-28, from https://onlinelibrary.wiley.com/doi/abs/10.1029/2023JC020563 (_eprint: https://onlinelibrary.wiley.com/doi/pdf/10.1029/2023JC020563) doi: 10.1029/2023JC020563

Mellor, G. L., & Yamada, T. (1982). Development of a turbulence closure model for geophysical fluid problems. *Reviews of Geophysics*, *20*(4), 851–875.

Moshonkin, S., & Harenduprakash, L. (1991). Effect of salinity and transparency on the mixed layer thermal structure in the bay of bengal. *Oceanology*, *31*, 384–394.

Nuijens, L., Wenegrat, J., Dekker, P. L., Pasquero, C., Neill, L. W. O., Ayet, A., ... Uchoa, I. (2023). The Air-Sea Interaction (ASI) submesoscale : physics and impact.

Paulson, C. A., & Simpson, J. J. (1977). Irradiance Measurements in the Upper Ocean. *Journal of Physical Oceanography*, *7*(6), 952–956. Retrieved from https://journals.ametsoc.org/view/journals/phoc/7/6/1520-0485_1977_007_0952_imituo_2_0_co_2.xml (Publisher: American Meteorological Society Place: Boston MA, USA) doi: 10.1175/1520-0485(1977)007⟨0952:IMITUO⟩2.0.CO;2

Phillips, H. E., Tandon, A., Furue, R., Hood, R., Ummenhofer, C. C., Benthuysen, J. A., ... Wiggert, J. (2021, November). Progress in understanding of Indian Ocean circulation, variability, air–sea exchange, and impacts on biogeochemistry. *Ocean Science*, *17*(6), 1677–1751. Retrieved 2025-04-26, from https://os.copernicus.org/articles/17/1677/2021/ doi: 10.5194/os-17-1677-2021

Pimentel, S., Tse, W.-H., Xu, H., Denaxa, D., Jansen, E., Korres, G., ... Storto, A. (2019). Modeling the Near-Surface Diurnal Cycle of Sea Surface Temperature in the Mediterranean Sea. *Journal of Geophysical Re-*

search: Oceans, *124*(1), 171–183. Retrieved 2025-05-28, from https://onlinelibrary.wiley.com/doi/abs/10.1029/2018JC014289 (_eprint: https://onlinelibrary.wiley.com/doi/pdf/10.1029/2018JC014289) doi: 10.1029/2018JC014289

Pradhan, M., Rao, S. A., Bhattacharya, A., & Balasubramanian, S. (2022). Improvements in Diurnal Cycle and Its Impact on Seasonal Mean by Incorporating COARE Flux Algorithm in CFS. *Frontiers in Climate*, *3*(February), 1–21. doi: 10.3389/fclim.2021.792980

Prytherch, J., Farrar, J. T., & Weller, R. A. (2013). Moored surface buoy observations of the diurnal warm layer. *Journal of Geophysical Research: Oceans*, *118*(9), 4553–4569. doi: 10.1002/jgrc.20360

Rao, R. R., Girish Kumar, M. S., Ravichandran, M., Rao, A. R., Gopalakrishna, V. V., & Thadathil, P. (2010). Interannual variability of Kelvin wave propagation in the wave guides of the equatorial Indian Ocean, the coastal Bay of Bengal and the southeastern Arabian Sea during 1993-2006. *Deep-Sea Research Part I: Oceanographic Research Papers*, *57*(1), 1–13. Retrieved from http://dx.doi.org/10.1016/j.dsr.2009.10.008 (Publisher: Elsevier) doi: 10.1016/j.dsr.2009.10.008

Rao, R. R., Jitendra, V., GirishKumar, M. S., Ravichandran, M., & Ramakrishna, S. S. (2015). Interannual variability of the Arabian Sea Warm Pool: observations and governing mechanisms. *Climate Dynamics*, *44*(7-8), 2119–2136. doi: 10.1007/s00382-014-2243-0

Rao, R. R., & Sivakumar, R. (1999). On the possible mechanisms of the evolution of a mini-warm pool during the pre-summer monsoon season and the genesis of onset vortex in the South-Eastern Arabian Sea. *Quarterly Journal of the Royal Meteorological Society*, *125*(555), 787–809. Retrieved 2025-05-31, from https://onlinelibrary.wiley.com/doi/abs/10.1002/qj.49712555503 (_eprint: https://rmets.onlinelibrary.wiley.com/doi/pdf/10.1002/qj.49712555503) doi: 10.1002/qj.49712555503

Rao, R. R., & Sivakumar, R. (2003, January). Seasonal variability of sea surface salinity and salt budget of the mixed layer of the north Indian Ocean. *Journal of Geophysical Research: Oceans*, *108*(C1), 9–14. Retrieved from https://doi

.org/10.1029/2001JC000907 (Publisher: John Wiley & Sons, Ltd) doi: https://doi.org/10.1029/2001JC000907

Renner, M., Wild, M., Schwarz, M., & Kleidon, A. (2019). Estimating Shortwave Clear-Sky Fluxes From Hourly Global Radiation Records by Quantile Regression. *Earth and Space Science*, *6*(8), 1532–1546. Retrieved 2025-06-08, from https://onlinelibrary.wiley.com/doi/abs/10.1029/2019EA000686 (_eprint: https://onlinelibrary.wiley.com/doi/pdf/10.1029/2019EA000686) doi: 10.1029/2019EA000686

Reynolds, R. W., Smith, T. M., Liu, C., Chelton, D. B., Casey, K. S., & Schlax, M. G. (2007, November). Daily High-Resolution-Blended Analyses for Sea Surface Temperature. Retrieved 2025-06-03, from https://journals.ametsoc.org/view/journals/clim/20/22/2007jcli1824.1.xml (Section: Journal of Climate) doi: 10.1175/2007JCLI1824.1

Roemmich, D., Johnson, G. C., Riser, S., Davis, R., Gilson, J., Owens, W. B., ... Ignaszewski, M. (2009). The Argo Program: Observing the Global Ocean with Profiling Floats. *Oceanography*, *22*(2), 34–43. Retrieved 2025-06-03, from https://www.jstor.org/stable/24860957 (Publisher: Oceanography Society)

Rudnick, D. L., & Weller, R. A. (1993). The heat budget in the North Atlantic subtropical frontal zone. *Journal of Geophysical Research: Oceans*, *98*(C4), 6883–6893. Retrieved 2025-06-08, from https://onlinelibrary.wiley.com/doi/abs/10.1029/92JC02885 (_eprint: https://onlinelibrary.wiley.com/doi/pdf/10.1029/92JC02885) doi: 10.1029/92JC02885

Schlosser, T. L., Lucas, A. J., Omand, M., & Farrar, J. T. (2022). Monsoons , plumes , and blooms : intraseasonal variability in the subsurface chlorophyll maximum in the Bay of Bengal.

Schlosser, T. L., Lucas, A. J., Omand, M., & Farrar, J. T. (2025). Monsoons, plumes, and blooms: intraseasonal variability of subsurface primary productivity in the Bay of Bengal. *EGUsphere*, *2025*, 1–25.

Seager, R., Zebiak, S. E., & Cane, M. A. (1988). A model of the tropical Pacific sea surface temperature climatology. *Journal of Geophysical Research: Oceans*, *93*(C2), 1265–1280. Retrieved 2025-05-28, from https://

onlinelibrary.wiley.com/doi/abs/10.1029/JC093iC02p01265 (_eprint: https://onlinelibrary.wiley.com/doi/pdf/10.1029/JC093iC02p01265) doi: 10.1029/JC093iC02p01265

Sengupta, D., Bharath Raj, G. N., Ravichandran, M., Sree Lekha, J., & Papa, F. (2016, May). Near-surface salinity and stratification in the north Bay of Bengal from moored observations. *Geophysical Research Letters*, *43*(9), 4448–4456. Retrieved from https://doi.org/10.1002/2016GL068339 (Publisher: John Wiley & Sons, Ltd) doi: https://doi.org/10.1002/2016GL068339

Sengupta, D., Bharath Raj, G. N., & Shenoi, S. S. C. (2006, November). Surface freshwater from Bay of Bengal runoff and Indonesian Throughflow in the tropical Indian Ocean. *Geophysical Research Letters*, *33*(22). Retrieved from https://doi.org/10.1029/2006GL027573 (Publisher: John Wiley & Sons, Ltd) doi: https://doi.org/10.1029/2006GL027573

Sengupta, D., Parampil, S. R., Bhat, G. S., Murty, V. S. N., Ramesh Babu, V., Sudhakar, T., ... Pradhan, Y. (2008). Warm pool thermodynamics from the Arabian Sea Monsoon Experiment (ARMEX). *Journal of Geophysical Research: Oceans*, *113*(C10). Retrieved 2025-05-31, from https://onlinelibrary.wiley.com/doi/abs/10.1029/2007JC004623 (_eprint: https://agupubs.onlinelibrary.wiley.com/doi/pdf/10.1029/2007JC004623) doi: 10.1029/2007JC004623

Sengupta, D., & Ravichandran, M. (2001, May). Oscillations of Bay of Bengal sea surface temperature during the 1998 Summer Monsoon. *Geophysical Research Letters*, *28*(10), 2033–2036. Retrieved from https://doi.org/10.1029/2000GL012548 (Publisher: John Wiley & Sons, Ltd) doi: https://doi.org/10.1029/2000GL012548

Sengupta, D., Ray, P. K., & Bhat, G. S. (2002). Spring Warming of the Eastern Arabian Sea and Bay of Bengal from Buoy Data. , *29*(15), 1–4.

Seo, H., O'Neill, L. W., Bourassa, M. A., Czaja, A., Drushka, K., Edson, J. B., ... Wang, Q. (2023). Ocean Mesoscale and Frontal-Scale Ocean-Atmosphere Interactions and Influence on Large-Scale Climate: A Review. *Journal of Climate*, *36*(7), 1981–2013. doi: 10.1175/JCLI-D-21-0982.1

Shenoi, S. S. C., Nasnodkar, N., Rajesh, G., Joseph, K. J., Suresh, I., & Almeida, A. M. (2009). On the diurnal ranges of Sea Surface Temperature (SST) in the

north Indian Ocean. *Journal of Earth System Science*, *118*(5), 483. (Publisher: Springer)

Shenoi, S. S. C., Shankar, D., & Shetye, S. R. (2002, June). Differences in heat budgets of the near-surface Arabian Sea and Bay of Bengal: Implications for the summer monsoon. *Journal of Geophysical Research: Oceans*, *107*(C6), 5–14. Retrieved from https://doi.org/10.1029/2000JC000679 (Publisher: John Wiley & Sons, Ltd) doi: https://doi.org/10.1029/2000JC000679

Shroyer, E. L., Rudnick, D. L., Farrar, J. T., Lim, B., Venayagamoorthy, S. K., St. Laurent, L. C., ... Moum, J. N. (2016, September). Modification of Upper-Ocean Temperature Structure by Subsurface Mixing in the Presence of Strong Salinity Stratification. *Oceanography*, *29*(2), 62–71. Retrieved from http://www.jstor.org/stable/24862670 (Publisher: Oceanography Society)

Sijikumar, S., & Rajeev, K. (2012, March). Role of the Arabian Sea Warm Pool on the Precipitation Characteristics during the Monsoon Onset Period. Retrieved 2025-05-31, from https://journals.ametsoc.org/view/journals/clim/25/6/jcli-d-11-00286.1.xml (Section: Journal of Climate) doi: 10.1175/JCLI-D-11-00286.1

Skyllingstad, E. D., Vickers, D., Mahrt, L., & Samelson, R. (2007, May). Effects of mesoscale sea-surface temperature fronts on the marine atmospheric boundary layer. *Boundary-Layer Meteorology*, *123*(2), 219–237. Retrieved 2025-05-14, from https://doi.org/10.1007/s10546-006-9127-8 doi: 10.1007/s10546-006-9127-8

Song, X., Xie, X., Qiu, B., Cao, H., Xie, S. P., Chen, Z., & Yu, W. (2022). Air-Sea Latent Heat Flux Anomalies Induced by Oceanic Submesoscale Processes: An Observational Case Study. *Frontiers in Marine Science*, *9*(March), 1–12. doi: 10.3389/fmars.2022.850207

Sprintall, J., & Tomczak, M. (1992). Evidence of the barrier layer in the surface layer of the tropics. *Journal of Geophysical Research: Oceans*, *97*(C5), 7305–7316. Retrieved 2025-05-31, from https://onlinelibrary.wiley.com/doi/abs/10.1029/92JC00407 (_eprint: https://agupubs.onlinelibrary.wiley.com/doi/pdf/10.1029/92JC00407) doi: 10.1029/92JC00407

964 Sree Lekha, J., Buckley, J. M., Tandon, A., & Sengupta, D. (2018). Subseasonal
965 dispersal of freshwater in the northern Bay of Bengal in the 2013 summer mon-
966 soon season. *Journal of Geophysical Research: Oceans*, *123*(9), 6330–6348.
967 Retrieved from https://doi.org/10.1029/2018JC014181 (Publisher: Wiley
968 Online Library)

969 Sree Lekha, J., Lucas, A. J., Sukhatme, J., Joseph, J. K., Ravichandran, M.,
970 Suresh Kumar, N., ... Sengupta, D. (2020). Quasi-Biweekly Mode of the
971 Asian Summer Monsoon Revealed in Bay of Bengal Surface Observations.
972 *Journal of Geophysical Research: Oceans*, *125*(12), e2020JC016271. Retrieved
973 from https://doi.org/10.1029/2020JC016271 (Publisher: Wiley Online
974 Library)

975 Stuart-Menteth, A. C., Robinson, I. S., & Challenor, P. G. (2003). A global study
976 of diurnal warming using satellite-derived sea surface temperature. *Journal of*
977 *Geophysical Research: Oceans*, *108*(C5). Retrieved 2025-05-31, from https://
978 onlinelibrary.wiley.com/doi/abs/10.1029/2002JC001534 (_eprint:
979 https://agupubs.onlinelibrary.wiley.com/doi/pdf/10.1029/2002JC001534) doi:
980 10.1029/2002JC001534

981 Sullivan, P. P., McWilliams, J. C., Weil, J. C., Patton, E. G., & Fernando, H. J. S.
982 (2020, December). Marine Boundary Layers above Heterogeneous SST: Across-
983 Front Winds. Retrieved 2025-05-14, from https://journals.ametsoc.org/
984 view/journals/atsc/77/12/jas-d-20-0062.1.xml (Section: Journal of the
985 Atmospheric Sciences) doi: 10.1175/JAS-D-20-0062.1

986 Sullivan, P. P., McWilliams, J. C., Weil, J. C., Patton, E. G., & Fernando, H. J. S.
987 (2021, October). Marine Boundary Layers above Heterogeneous SST:
988 Alongfront Winds. Retrieved 2025-05-14, from https://journals.ametsoc
989 .org/view/journals/atsc/78/10/JAS-D-21-0072.1.xml (Section: Journal
990 of the Atmospheric Sciences) doi: 10.1175/JAS-D-21-0072.1

991 Sun, C., Zhang, A., Jin, B., Wang, X., Zhang, X., & Zhang, L. (2022, Novem-
992 ber). Seasonal variability of eddy kinetic energy in the north Indian
993 Ocean. *Frontiers in Marine Science*, *9*. Retrieved 2025-06-05, from
994 https://www.frontiersin.org/journals/marine-science/articles/
995 10.3389/fmars.2022.1032699/full (Publisher: Frontiers) doi: 10.3389/
996 fmars.2022.1032699

997 Thangaprakash, V. P., Suprit, K., Kumar, N. S., & Chaudhuri, D. (2016, July).
998 What Controls Seasonal Evolution of Sea Surface Temperature in the Bay
999 of Bengal? Mixed Layer Heat Budget Analysis Using Moored Buoy Obser-
1000 vations.... *Oceanography*, *29*(2), 202–213. Retrieved 2025-06-05, from
1001 https://tos.org/oceanography/article/what-controls-seasonal
1002 -evolution-of-sea-surface-temperature-in-the-bay-of-b doi:
1003 10.5670/oceanog.2016.52

1004 Thompson, E. J., Moum, J. N., Fairall, C. W., & Rutledge, S. A. (2019). Wind
1005 Limits on Rain Layers and Diurnal Warm Layers. *Journal of Geophysical Re-*
1006 *search: Oceans*, *124*(2), 897–924. doi: 10.1029/2018JC014130

1007 Vinayachandran, P. N., & Nanjundiah, R. S. (2009). Indian Ocean sea surface salin-
1008 ity variations in a coupled model. *Climate dynamics*, *33*, 245–263. (Publisher:
1009 Springer)

1010 Vinayachandran, P. N., Shankar, D., Kurian, J., Durand, F., & Shenoi, S. S. (2007).
1011 Arabian Sea mini warm pool and the monsoon onset vortex. *Current Science*,
1012 *93*(2), 203–214.

1013 Vinayachandran, P. N., & Shetye, S. R. (1991, June). The warm pool in the In-
1014 dian Ocean. *Proceedings of the Indian Academy of Sciences - Earth and Plane-*
1015 *tary Sciences*, *100*(2), 165–175. Retrieved 2025-05-31, from https://doi.org/
1016 10.1007/BF02839431 doi: 10.1007/BF02839431

1017 Weller, R. A., Baumgartner, M. F., Josey, S. A., Fischer, A. S., & Kindle, J. C.
1018 (1998, August). Atmospheric forcing in the Arabian Sea during 1994–1995:
1019 observations and comparisons with climatology and models. *Deep Sea Re-*
1020 *search Part II: Topical Studies in Oceanography*, *45*(10), 1961–1999. Retrieved
1021 2025-05-30, from https://www.sciencedirect.com/science/article/pii/
1022 S0967064598000605 doi: 10.1016/S0967-0645(98)00060-5

1023 Weller, R. A., Farrar, J. T., Buckley, J., Mathew, S., Venkatesan, R., Lekha, J. S.,
1024 ... Kumar, B. P. (2016, September). Air-Sea Interaction in the Bay of Bengal.
1025 *Oceanography*, *29*(2), 28–37. Retrieved from http://www.jstor.org/stable/
1026 24862667 (Publisher: Oceanography Society)

1027 Weller, R. A., Farrar, J. T., Seo, H., Prend, C., Sengupta, D., Sree Lekha, J., ...
1028 Venkatesen, R. (2019). Moored observations of the surface meteorology and
1029 air-sea fluxes in the northern bay of Bengal in 2015. *Journal of Climate*, *32*(2),

549–573. doi: 10.1175/JCLI-D-18-0413.1

Weller, R. A., Fischer, A. S., Rudnick, D. L., Eriksen, C. C., Dickey, T. D., Marra, J., ... Leben, R. (2002, January). Moored observations of upper-ocean response to the monsoons in the Arabian Sea during 1994–1995. *Deep Sea Research Part II: Topical Studies in Oceanography*, *49*(12), 2195–2230. Retrieved 2025-05-30, from https://www.sciencedirect.com/science/article/pii/S0967064502000358 doi: 10.1016/S0967-0645(02)00035-8

Wentz, F. J., Meissner, T., Gentemann, C., Hilburn, K. A., & Scott, J. (2014). *Remote Sensing Systems GCOM-W1 AMSR2 Daily Environmental Suite on 0.25 deg grid, Version 8.2,.* (Place: Santa Rosa, CA Medium: Remote Sensing Systems)

Wijesekera, H. W., Shroyer, E., Tandon, A., Ravichandran, M., Sengupta, D., Jinadasa, S. U. P., ... Whalen, C. B. (2016). ASIRI: An Ocean–Atmosphere Initiative for Bay of Bengal. *Bulletin of the American Meteorological Society*, *97*(10), 1859–1884. Retrieved from https://journals.ametsoc.org/view/journals/bams/97/10/bams-d-14-00197.1.xml (Publisher: American Meteorological Society Place: Boston MA, USA) doi: 10.1175/BAMS-D-14-00197.1

Witte, C. R., Subramaniam, A., & Zappa, C. J. (2024). An Improved Bio-Physical Parameterization for Ocean Radiant Heating in Conditions of Near-Surface Stratification. *Journal of Geophysical Research: Oceans*, *129*(11), e2024JC021049. Retrieved 2025-05-27, from https://onlinelibrary.wiley.com/doi/abs/10.1029/2024JC021049 (_eprint: https://agupubs.onlinelibrary.wiley.com/doi/pdf/10.1029/2024JC021049) doi: 10.1029/2024JC021049

Yuan, X., Yu, X., & Su, Z. (2020, October). Seasonal and interannual variabilities of the barrier layer thickness in the tropical Indian Ocean. *Ocean Science*, *16*(5), 1285–1296. Retrieved 2025-05-31, from https://os.copernicus.org/articles/16/1285/2020/ (Publisher: Copernicus GmbH) doi: 10.5194/os-16-1285-2020